

Potential vegetation changes in the permafrost areas over the Tibetan Plateau under future climate warming

Rui Chen^{1,2}, Jan Nitzbon¹, Thomas Schneider von Deimling¹, Simone Maria Stuenzi¹, Ngai-Ham Chan¹, Julia Boike^{1,2}, and Moritz Langer^{1,3}

¹Permafrost Research Section, Alfred Wegener Institute Helmholtz Centre for Polar and Marine Research,

Potsdam, Germany

²Geography Department, Humboldt-Universität zu Berlin, Berlin, Germany

³Department of Earth Sciences, Vrije Universiteit Amsterdam, Amsterdam, the Netherlands

Key Points:

- By 2100, the permafrost areas will thaw at 0.23 ± 0.04 and $0.60 \pm 0.02 \times 10^6 \text{ km}^2$ under SSP1–2.6 and SSP5–8.5, respectively.
- By 2050, NDVI in the permafrost areas likely stay stable under SSP1–2.6 scenarios and likely show a rising trend under SSP5–8.5 scenarios.
- Surface air temperature and liquid water content at the root zone are the dominant features affecting NDVI changes in the permafrost areas.

16 **Abstract**

17 Permafrost degradation on the Tibetan Plateau is well-documented and expected to con-
 18 tinue throughout this century. However, the impact of thawing permafrost on the dis-
 19 tribution, composition, and resilience of vegetation communities in this region is not well
 20 understood. In this study, we combined a transient numerical permafrost model with ma-
 21 chine learning algorithms to project the near-future thermal state of permafrost and veg-
 22 etation (represented by the Normalized Difference Vegetation Index [NDVI]) changes un-
 23 der two contrasting climate pathways (Shared Socioeconomic Pathway 1–2.6 [SSP1–2.6]
 24 and SSP5–8.5). The contribution of climatic and terrestrial variables to vegetation evo-
 25 lution was quantified using ridge regression. By 2100, permafrost areas were expected
 26 to decrease by $21 \pm 4\%$, and $55 \pm 2\%$ under the SSP1–2.6 and SSP5–8.5 scenarios, respec-
 27 tively, relative to the baseline period (2000–2018). Under the SSP1–2.6 scenarios, the
 28 mean annual ground temperature and active layer thickness were projected to fluctuate
 29 stably, while under the SSP5–8.5 scenarios, a significant increasing trend was anticipated.
 30 Satellite-based observations indicated an increasing trend of NDVI within the permafrost
 31 areas from 2000 to 2018 (0.01 per decade), mainly attributed to climatic factors. In the
 32 future, vegetation greenness was expected to possibly remain stable under SSP1–2.6 sce-
 33 narios, whereas a rising trend was likely noted under SSP5–8.5 scenarios during 2019–
 34 2050, mainly controlled by the surface air temperature and liquid water content at the
 35 root zone during the growing season. Our modeling work provides a potential approach
 36 for investigating future vegetation changes and offers more possibilities to improve un-
 37 derstanding of the interaction between soil-vegetation-atmosphere in cold regions.

38 **Plain Language Summary**

39 About 40% of the Tibetan Plateau is underlain by permafrost, which has under-
 40 gone significant degradation and is estimated to experience substantial thawing by the
 41 end of this century. The thawing permafrost has impacted vegetation growth. To date,
 42 it has not been clear how the Normalized Difference Vegetation Index (NDVI; represent-
 43 ing vegetation) changes with climate warming and permafrost degradation. Here, we used
 44 a land surface model and machine learning algorithms to simulate future permafrost ther-
 45 mal regimes and variations in the NDVI for future growing seasons and assess the most
 46 important variables influencing NDVI variability. We found that permafrost areas were
 47 projected to shrink by $21 \pm 4\%$ under the SSP1–2.6 scenarios and $55 \pm 2\%$ under the SSP5–
 48 8.5 scenarios by 2100, compared to the baseline period (2000–2018). Our results suggested
 49 that under mild climate conditions (SSP1–2.6), NDVI in the permafrost areas likely re-
 50 mained stable from 2019 to 2050, while NDVI in the permafrost areas likely showed an
 51 increasing trend under harsh climate conditions (SSP5–8.5), which was mainly due to
 52 increasing surface air temperature and liquid water content at the root zone on the Ti-
 53 betan Plateau.

54 **1 Introduction**

55 The Tibetan Plateau (TP; Figure 1) hosts the world's most extensive high-altitude
 56 permafrost areas, estimated at $1.15 \times 10^6 \text{ km}^2$ (2005–2015) (Ran et al., 2021). Previous
 57 studies showed that permafrost had undergone significant degradation due to anthro-
 58 pogenic warming (Smith et al., 2022; X. Wang et al., 2022; Baral et al., 2023), as evi-
 59 denced by increased mean annual ground temperature (MAGT) (Q. Wu & Zhang, 2008;
 60 Zhao et al., 2021), increased active layer thickness (ALT) (Q. Wu & Zhang, 2010; Qin
 61 et al., 2017), reduced permafrost thickness and areas (D. Guo & Wang, 2013; Ran et al.,
 62 2018), and altered geomorphological features (T. Gao et al., 2021; Xia et al., 2022). Ac-
 63 cording to state-of-the-art Earth System Models (ESMs), the mean annual surface air
 64 temperature over the TP is projected to rise by 1.9°C under the Shared Socioeconomic
 65 Pathway 1–2.6 (SSP1–2.6) and by as much as 6.3°C under SSP5–8.5 by the end of the

66 21st century, relative to the baseline period of 1981–2010 (R. Chen, Li, et al., 2022). Such
 67 warming is expected to exacerbate the thawing and warming of the permafrost. Com-
 68 pared to the baseline period (2006–2015), the MAGT and ALT are estimated to increase
 69 by 0.8°C to 2.6°C and 0.7 m to 3.0 m , respectively, in the period 2091–2100 under the
 70 SSP2–4.5 to SSP5–8.5 scenarios (G. Zhang et al., 2022), corresponding with a decline
 71 in permafrost areas by 44% to 71% (G. Zhang et al., 2022). This degradation is expected
 72 to cause major impacts on the carbon budget (Mu et al., 2020; T. Wang et al., 2020),
 73 hydrological dynamics (Song et al., 2022; T. Wang et al., 2023), ecosystem (Cuo et al.,
 74 2022; T. Wang et al., 2022), and infrastructure stability (Ran, Cheng, et al., 2022; R. Chen
 75 et al., 2023) on the regional scale. Vegetation covers approximately 81 % of the permafrost
 76 areas on the TP, rendering it the predominant surface characteristic (Z. Wang et al., 2016).
 77 With methodological innovations, sophisticated models, and a surge in observational data,
 78 our understanding of permafrost–vegetation interactions is improving (Heijmans et al.,
 79 2022). On the one hand, vegetation significantly influences the hydrothermal regime, car-
 80 bon, and nutrient dynamics in permafrost environments. This influence is exerted through
 81 alterations in the surface energy balance (Chang et al., 2015; Stuenzi, Boike, Cable, et
 82 al., 2021), regulation of snow cover dynamics (Lawrence & Swenson, 2011; Grünberg et
 83 al., 2020), and impacts on both ecosystem carbon uptake (Ding et al., 2017; D. Wei et
 84 al., 2021) and ecosystem respiration processes (Gagnon et al., 2019; Prager et al., 2020).
 85 On the other hand, the evolution of permafrost significantly affects vegetation patterns,
 86 either promoting greening or browning (Myers-Smith et al., 2020). This is primarily me-
 87 diated by its control over soil temperature and liquid water content in the root zone (Yi
 88 et al., 2014; de Vrese et al., 2023), alterations in landscape morphology (van der Kolk
 89 et al., 2016; Mu et al., 2017; Loranty et al., 2018), impacts on microbial stability (M. Wu
 90 et al., 2021), and influences on carbon and nitrogen cycling processes (Mekonnen et al.,
 91 2018; L. Liu et al., 2022; Mauclet et al., 2022).

92 Continuous vegetation greening and enhanced carbon uptake were also observed
 93 on the TP along with climate warming and permafrost degradation since the 1980s (Teng
 94 et al., 2021; Cuo et al., 2022; Shi et al., 2023; Z. Jin et al., 2023; Y. Wang et al., 2023).
 95 Notably, the Normalized Difference Vegetation Index (NDVI) exhibited an upward trend
 96 of 0.011 per decade from 1982 to 2015 (Teng et al., 2021). Similarly, the Enhanced Veg-
 97 etation Index (EVI; which was developed to optimize the vegetation signal with improved
 98 sensitivity in high-biomass regions) increased by 0.01 per decade from 2000 to 2020 (Shi
 99 et al., 2023), and the Net Primary Productivity (NPP) demonstrated a positive trend
 100 of 0.51 g C m^{-2} per decade from 1982 to 2014 (Cuo et al., 2022). While many studies
 101 have identified warming temperatures and increasing precipitation to be the main drives
 102 of greening (Teng et al., 2021; X. Li et al., 2022; T. Wang et al., 2022) and plant phe-
 103 nology changes (Q. Zhang et al., 2018; M. Shen et al., 2022; T. Wang et al., 2022) across
 104 the TP, vegetation greening on the global scale is thought to be mainly induced by CO_2
 105 fertilization (Piao et al., 2020). In addition to the climatic factors, the hydrothermal con-
 106 ditions of the permafrost would also affect the vegetation dynamics through the permafrost-
 107 vegetation interactions (J. Wang & Liu, 2022; T. Wang et al., 2022). All of these stud-
 108 ies have significantly improved our understanding of the characteristics and drivers of
 109 the vegetation greenness on the TP. However, it is still largely unknown how the veg-
 110 etation cover will evolve under further destabilizing permafrost conditions on the TP ac-
 111 counting for future climate scenarios at a larger spatial scale. This uncertainty persists
 112 since the very complex vegetation physiological processes which are often tied to spe-
 113 cific local conditions are not yet well represented in generalistic ESMs (Piao et al., 2020).
 114 With machine learning approaches increasingly being used to analyze complex spatiotem-
 115 poral data and explore future environmental change (Pearson et al., 2013; Nitze et al.,
 116 2018; J. Guo et al., 2023; C. Shen et al., 2023), coupling the model-based and data-driven
 117 methods allows us to deal with the complex permafrost–vegetation interactions and quan-
 118 tify the vegetation dynamics and its dominant factors under different climate scenarios.

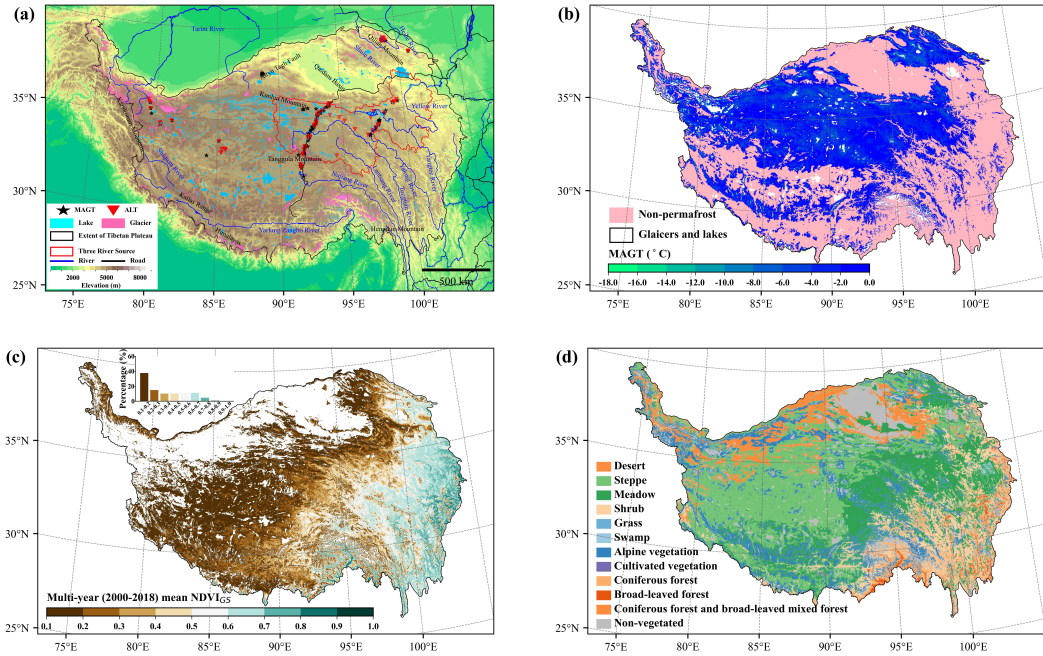


Figure 1. (a) Topography of study areas and location of observation sites over the Tibetan Plateau. Black stars and red triangles stand for the mean annual ground temperature (MAGT) and active layer thickness (ALT) of the monitoring sites, respectively. The digital elevation model, glacier, lake, river, and the boundary of the Tibetan Plateau data and the boundary of Three River Sources are obtained from the National Tibetan Plateau Data Center <https://data.tpdc.ac.cn> and are licensed under CC BY 4.0. The road data is available from the national 1:1000000 public basic geographic database of China (version 2017). (b) Spatial distributions of permafrost and non-permafrost areas on the Tibetan Plateau. Data source: (Obu et al., 2019). (c) Spatial distribution of the multi-year (2000–2018) mean of the growing season (May to September) NDVI on the Tibetan Plateau at 1km² scale from MODIS satellite imagery, the sub barplot represents the percentage of the number of grid cells of NDVI in each interval to the total number of grid cells. (d) Maps of vegetation types in the Tibetan Plateau adapted from the 1:1000000 vegetation map of China (Zhou et al., 2022)

In this study, we combined a physically-based permafrost model (CryoGridLite) (Langer et al., 2024) and machine-learning approaches for predicting the vegetation evolution (represented by the NDVI) over the permafrost areas on the TP. Firstly, we applied the CryoGridLite, driven by historical and future forcing datasets under the two different SSPs scenarios (SSP1–2.6 and SSP5–8.5) from two ESMs (AWI-CM-1-1-MR and MPI-ESM1-2-HR), to assess the potential shifts in permafrost distribution and its thermal state over the TP. Then, based on the output of the CryoGridLite model, we used machine-learning algorithms, which are Light Gradient Boosting Machine (Light-GBM) (Ke et al., 2017) and Extreme Gradient Boosting Machine (XGBoost) (T. Chen & Guestrin, 2016), to quantify the prospective changes in NDVI within the permafrost areas of the TP. Finally, we elucidated the dominant factors influencing NDVI variations and quantified the contribution of each explanatory variable to the NDVI change.

131 **2 Methods**

132 **2.1 CryoGridLite**

133 We applied the one-dimensional transient permafrost model CryoGridLite (Langer
 134 et al., 2024) to simulate the trajectory of permafrost evolution over the TP. CryoGridLite
 135 was a fast version that was inherited from CryoGrid3 (Westermann et al., 2016) and the
 136 CryoGrid community model (Westermann et al., 2023), reducing computational costs
 137 and thus making it more suitable for regional (e.g., TP) to hemispherical scale (e.g., Pan-
 138 Arctic; Nitzbon et al. (2023)) permafrost modeling. In the following, we briefly describe
 139 the main aspects of CryoGridLite and provide the model setup for this work. Further
 140 detailed descriptions of model structures and physical processes can be found in Langer
 141 et al. (2024).

142 **2.1.1 Model description**

143 In this tailored version of CryoGridLite, we implemented the surface energy bal-
 144 ance module, which was driven by the time series of forcing data (i.e. surface air tem-
 145 perature ($^{\circ}C$), rainfall and snowfall rate ($m\ h^{-1}$), ($kg\ kg^{-1}$), surface air pressure (Pa),
 146 incoming shortwave and longwave radiation ($W\ m^{-1}$), and wind ($m\ s^{-1}$)), to provide the
 147 upper boundary condition of the model (detailed description can be seen in Supporting
 148 Information Text S1.1). Unlike the heat condition equation implemented in CryoGrid3,
 149 the CryoGridLite used enthalpy instead of temperature as the state variable to solve the
 150 one-dimensional subsurface heat transfer:

$$\frac{\partial H}{\partial t} - \frac{\partial}{\partial z}(k(z, T)\frac{\partial T(H)}{\partial z}) = 0 \quad (1)$$

151 where $H (J\ m^{-3})$ is the volumetric enthalpy including sensible and latent heat contents
 152 of the ground, $t (s)$ is time, $z (m)$ is the vertical subsurface depth, $k (z, T)(W\ m^{-1}\ K^{-1})$
 153 is the effective thermal conductivity derived from volumetric soil fractions of mineral,
 154 organic, water, ice and air in a given soil depth, and $T (k)$ is the ground temperature.
 155 The lower boundary condition was defined by constant geothermal heat flux. The im-
 156 plemented snowpack scheme allowed the model to simulate snow accumulation, ablation,
 157 melt-water routing, and refreezing within the snow cover. Once the snow had filled the
 158 first grid cell above the soil surface, the surface albedo changed from that of the soil to
 159 that of the fresh snow and decreased over time towards that of the albedo of old snow
 160 (Westermann et al., 2016). Besides, we applied a simple bucket scheme (a detailed de-
 161 scription can be seen in Supporting Information Text S1.2) with only downward verti-
 162 cal water flow driven by gravity to compute the dynamics of soil water content rather
 163 than constant water contents used in (Langer et al., 2024).

164 **2.1.2 Model setup**

165 In this study, we synthesized the China Meteorological Forcing dataset (CMFD;
 166 selected period: 1979–2018 to represent historical climate conditions; resolution: 3 hours
 167 and $0.1^{\circ} \times 0.1^{\circ}$) (He et al. (2020); <https://www.tpdc.ac.cn>), along with two ESMs
 168 from CMIP6 (AWI-CM-1-1-MR and MPI-ESM1-2-HR; selected period: 2019–2100 to
 169 portray future climate conditions; resolution: monthly and $0.9375^{\circ} \times 0.9375^{\circ}$) (Müller
 170 et al. (2018); Semmler et al. (2020); <https://esgf-data.dkrz.de>) following the two
 171 SSP scenarios (SSP1–2.6 and SSP5–8.5) to construct the completely forcing data (pe-
 172 riod: 1979–2100; resolution: hourly and $0.1^{\circ} \times 0.1^{\circ}$). Compared with other ESMs, AWI-
 173 CM-1-1-MR, and MPI-ESM1-2-HR presented the best performance in depicting the spa-
 174 tiotemporal patterns of mean annual and seasonal surface air temperature on the TP
 175 in the past decades (R. Chen, Li, et al., 2022). To ensure model stability and consistency
 176 of the forcing data from 1979 to 2100, we performed a linear interpolation on the CMFD
 177 data from a 3-hour to an hourly resolution. Further, we utilized the approach from Westermann
 178 et al. (2016) by combining baseline climate data (from CMFD) with monthly climate anom-

lies (from ESMs) to generate the forcing data for this study. The time series of all forcing variables under the two SSPs and two ESMs for the period 1979–2100 is shown in Supporting Information Figure S1.

For the soil domain of the model, the vertical resolution of grid cells increased with thickness from the soil surface (0m) to the lower boundary of the model (100m) (0.02m in 0–2m depth; 0.05m in 2–4m depth; 0.1m in 4–10m depth; 0.2m in 10–20m depth; 1m in 20–30m depth; 5m in 30–50m depth; 10m in 50–100m depth). The soil stratigraphies were specified as mineral, organic, initial water/ice, and air volumetric fractions. The initial water/ice content according to Langer et al. (2023) was assumed halfway between field capacity and porosity for the soil layer above the water table depth, which was provided by a global groundwater table depths product (Fan et al. (2013); <https://thredds-gfnl.usc.es/thredds/catalog/GLOBALWTDFTP/catalog.html>), and saturated with the soil layer below the water table depth. The soil properties were derived from a new version of the global high-resolution dataset of soil hydraulic and thermal parameters dataset for land surface modeling (Y. Dai, Xin, et al. (2019); Y. Dai, Wei, et al. (2019); <https://globalchange.bnu.edu.cn>). The spatial resolution of this dataset was 0.00833° covering from 90° N to 90° S, 180° W to 180° E, and the vertical soil profile was provided in 8 layers (0–0.0451m, 0.0451–0.0906m, 0.0906–0.1655m, 0.1655–0.2891m, 0.2891–0.4929m, 0.4929–0.8289m, 0.8289–1.3828m and 1.3828–3.8019m). This dataset directly provided the volumetric fraction of soil organic matter and soil porosity. At the same time, mineral content and field capacity were calculated based on the approach in Y. Dai et al. (2013); Y. Dai, Xin, et al. (2019); Y. Dai, Wei, et al. (2019). Besides, we assumed the soil stratigraphy from 3.8019m to the bedrock depth Yan et al. (2020) was the same as that of the soil layer above it (i.e. 1.3828–3.8019m). Below the bedrock depth, we assumed no soil organic matter existed, the soil porosity was arbitrarily set to 0.1, and the soil mineral content was set to 0.9. We utilized the geothermal gradient ($0.031^{\circ}C\text{ m}^{-1}$; Y. Pang et al. (2022)) to interpolate the four-layer ERA5Land soil temperature (Muñoz-Sabater et al., 2021) in January 1979 to the whole soil profile as the initial ground temperature profile. The constant geothermal heat flux was extracted from the Terrestrial Heat Flow Dataset Lucaleau (2019) to describe the lower boundary condition.

To depict snowpack dynamics over time, five empty grid cells were set above the soil surface in the initial state to represent the maximum snow depth of 0.1m with a vertical resolution of 0.02m (Orsolini et al., 2019). We assumed a constant snow density (150 kg m^{-3}) across the snowpack (L. Dai et al., 2018; Yin et al., 2021) and the fresh snow albedo was set to 0.82 (W. Wang et al., 2020). The parameters used in this study for model setup are summarized in the Supporting Information Table S1. We applied nearest-neighbor interpolation for all input datasets (detailed information is provided in Table 1) and further masked them with shape files of the boundary (Y. Zhang et al. (2014); <https://www.geodoi.ac.cn>), glaciers (W. Guo et al. (2015); <https://www.tpdc.ac.cn>), and lakes (G. Zhang et al. (2019); <https://www.tpdc.ac.cn>) of the TP to finalize the model setup for each grid cell in our simulations.

2.2 Machine learning model

In this study, we adopted two regression-based machine learning approaches to project the future NDVI change on the permafrost areas over the TP, which have been widely used in the prediction of future climate as well as environmental variables (Ukkonen & Mäkelä, 2019; Kondylatos et al., 2022; F. Chen et al., 2023; Veigel et al., 2023; C. Chen et al., 2024). The NDVI was collected from the Moderate Resolution Imaging Spectroradiometer (MODIS; MOD13A2; Didan (2015)) with a 1km spatial resolution from 2000–2018 to match up the period of CMFD and be regarded as the baseline period in this study. We processed the raw NDVI data to aggregate them into monthly intervals, which was the time resolution used in our machine learning approaches, using the maximum value composition approach (G. Pang et al., 2022) and further applied a Savitzky-Golay

Table 1. Overview of datasets used in this study

Datasets	Variable/Parameter	Reference/Source	Comments
China Meteorological Forcing Dataset	meteorological forcing	He et al. (2020)	Historical forcing 1979–2018
AWI-CM-1-1-MR MPI-ESM1-2-HR	meteorological forcing	Semmler et al. (2020) Müller et al. (2018)	Future forcing 2019–2100
Global high-resolution dataset of soil hydraulic and thermal parameters	Volumetric fractions of mineral, organic, porosity, and field capacity	Y. Dai, Xin, et al. (2019) Y. Dai, Wei, et al. (2019)	Soil stratigraphy
Global water-table depth dataset	Watertable depth	Fan et al. (2013)	Used to determine initial water/ice content
Terrestrial Heat Flow Dataset	Geothermal heat flux	Lucazeau (2019)	Lower boundary conditions
A Global Depth to Bedrock Dataset for Earth System Modeling	Bedrock depth	Yan et al. (2020)	Used to constrain soil depth
ERA5-Land	Four-layer soil temperature	Muñoz-Sabater et al. (2021)	Initial soil temperature
MODIS NDVI (MOD13A2, Version 6.1, 1km spatial resolution)	NDVI	Didan (2015)	Vegetation condition
Vegetation map from a digitized 1:1000000 vegetation atlas of China	Vegetation types	Zhou et al. (2022)	Analyzing NDVI changes and driving factors across various vegetation types

filter to smooth the NDVI time series (T. Wang et al., 2022). In addition, we assumed that there was no vegetation in the area with a multi-year (2000–2018) average growing season NDVI (from May to September, NDVI_{GS} ; Teng et al. (2021)) lower than 0.1 (T. Wang et al., 2022). The spatiotemporal trend of NDVI_{GS} over the TP (excluding the non-vegetation areas) from 2000 to 2018 based on the MODIS dataset is shown in the Supporting Information Figure S2. We incorporated six variables as explanatory factors in the machine-learning model based on previous studies (J. Wang & Liu, 2022; T. Wang et al., 2022; Y. Wang et al., 2023). Among them, surface air temperature (SAT), total precipitation (PRE), and incoming shortwave radiation (SIN) originated from climate-forcing data. Furthermore, the soil temperature (ST) and liquid water content (LWC) at the root zone (0–20cm; T. Wang et al. (2022)), and ALT are derived from the output of the CryoGridLite model for each grid cell. The time interval of these six variables was monthly, corresponding with the temporal resolution of the NDVI. The flow of the machine learning approach was as follows: First, the MODIS NDVI dataset and six explanatory variables that correspond with the same grid cell were divided into two groups: data from 2000 to 2014 served as the training dataset (about 80% of the data), and the remaining data (2015–2018) as the testing dataset (about 20% of the data). Then, according to the results from the CryoGridLite in the baseline period, we constructed the training and testing datasets on permafrost and non-permafrost areas (excluded ALT). For tuning the hyperparameters of each machine learning model in the training dataset in each area, we used Bayesian optimization (Python; Optuna package) with 500 iterations and set the early stopping and pruning strategy. The range of possible values for the part of hyperparameters and the final best hyperparameters can be seen in the Supporting Information Table S2. In each iteration, we used mean squared error as a scoring criterion and performed 5-fold cross-validation using the TimeSeriesSplit (Python; Scikit-learn package) approach due to there being a time dependence within the NDVI data. The optimal model parameter combinations resulting from each iteration were recorded and utilized to train the final model. Moreover, we introduced a weighting parameter for each model to enhance the model's emphasis on the growing season NDVI_{GS} associated with individual grid cells. In comparison to the monthly NDVI values, our preference was for the model to exhibit superior performance when modeling the NDVI_{GS} value. Similar to the hyperparameters used for each model, this weighting parameter was employed to obtain the optimal solution during the Bayesian optimization process. To evaluate the performance of each model, we employed root mean squared error (RMSE), bias (BIAS), coefficient of determination (R^2), and Kling-Gupta efficiency (KGE; Gupta et al. (2009)) as the evaluation metrics.

$$RMSE = \sqrt{\frac{1}{N} \sum_{i=1}^N (S_i - O_i)^2} \quad (2)$$

$$BIAS = \frac{1}{n} \sum_{i=1}^n (S_i - O_i) \quad (3)$$

$$R^2 = 1 - \frac{\sum_{i=1}^n (S_i - O_i)^2}{\sum_{i=1}^n (O_i - \bar{O})^2} \quad (4)$$

$$KGE = 1 - \sqrt{(r - 1)^2 + \left(\frac{S}{O} - 1\right)^2 + \left(\frac{\sigma_S}{\sigma_O} - 1\right)^2} \quad (5)$$

where N is the number of validation data, S_i and O_i ($i = 1, 2, \dots, N$) are the values of simulated and observed data, respectively, S and O are the mean values of simulated and observed data, respectively, r is the Pearson correlation coefficient, σ_S , and σ_O are the standard deviations of simulated and observed data, respectively. We utilized the optimal machine learning model and future explanatory data to produce the NDVI for each grid cell within the permafrost and non-permafrost region over the TP.

273 **2.3 Statistical analysis**

274 We employed three indices including the MAGT ($^{\circ}C$), ALT (m), and permafrost
 275 areas (km^2) to quantify permafrost degradation. In this study, we obtained the MAGT
 276 from the depth of zero annual amplitude, which was typically at the 10–15m soil depth
 277 on the TP (Q. Wu & Zhang, 2010; Qin et al., 2017). We defined a grid cell as permafrost
 278 if its MAGT lies below the $0^{\circ}C$ isotherm at the specific year (Ran, Li, et al., 2022). The
 279 ALT was quantified as the maximum thaw depth within the upper 10m of the subsur-
 280 face (Langer et al., 2024) and there is no existing ALT and permafrost when the MAGT
 281 exceeds $0^{\circ}C$ at the specific year at a grid cell. We employed the Albers Equal Area pro-
 282 jection for area calculations to accurately represent permafrost areas. To better track
 283 the dynamics of vegetation conditions across the permafrost and non-permafrost areas
 284 on the TP, we used the annual $NDVI_{GS}$ to represent the vegetation at individual years
 285 for each grid cell. In this study, we used ridge regression to robustly estimate the indi-
 286 vidual contributions of explanatory variables (mean or sum value at the growing season,
 287 i.e. SAT_{GS} , PRE_{GS} , SIN_{GS} , ST_{GS} , LWC_{GS} , and ALT_{GS}) to the variability in annual
 288 $NDVI_{GS}$ across the permafrost and non-permafrost region (T. Wang et al., 2022; J. Li
 289 et al., 2023). This approach effectively mitigated the issue of multicollinearity inherent
 290 among the predictors. The incorporation of a regularization penalty term (λ) served to
 291 apportion variance across the coefficients efficiently, thereby enhancing the precision of
 292 the estimated impacts of the explanatory variables on $NDVI_{GS}$. Preceding the regres-
 293 sion analysis, standardized explanatory variables and corresponding $NDVI_{GS}$ served as
 294 inputs for the ridge regression model. The optimal regularization parameter, λ , was sys-
 295 tematically determined through 5-fold cross-validation and the Grid Search algorithm,
 296 ensuring the most robust model performance. Variables exhibiting the largest absolute
 297 values of the regression coefficients post-regularization were interpreted as the dominant
 298 factors influencing $NDVI_{GS}$ within the specific grid cells. A comprehensive range of the
 299 λ values explored during the model tuning phase was from 1×10^{-6} to 1×10^6 . Besides,
 300 trend estimations of time series in this study were based on Sen's slope, which was se-
 301 lected over linear regression for its robustness against outliers and its nonparametric na-
 302 ture (Y. Wang et al., 2023). The flowchart of this study is shown in Figure 2.

303 **3 Results**304 **3.1 Model evaluations**305 **3.1.1 CryoGridLite**

306 For this study, we synthesized observational data, including MAGT and ALT, from
 307 a range of literature and public resources across the TP to assess the effectiveness of the
 308 CryoGridLite model (Q. Wu et al., 2020; H. Chen et al., 2015; J. Chen et al., 2016; Qin
 309 et al., 2017; Luo et al., 2018; Z. Zhang et al., 2020; Zhao et al., 2021; Mu & Peng, 2022;
 310 Y. Gao et al., 2023). Ultimately, we selected a total of $n_{MAGT} = 84$ and $n_{ALT} = 66$
 311 different grid cells comprising 151 MAGT and 86 ALT data records within various per-
 312 mafrost regions of the TP from 2000 to 2015 in our model domain (Detailed informa-
 313 tion see Supporting Information Table S3). Figure 1 (a) displays the geographical dis-
 314 tribution of these sites across the TP. For MAGT, we utilized the model output at the
 315 depth closest to the measured for comparison while for ALT, we considered the annual
 316 maximum thaw depth to compare the observed. Our modeling results indicated the sim-
 317 ulated MAGT at most sites (53.6 %) in the range of $\pm 1^{\circ}C$ of the observed value (Figure
 318 3 (a)), and there was a positive correlation between simulated and observed MAGT
 319 (Pearson correlation coefficient = 0.46, $p < 0.01$). However, we noted that our model
 320 tended to underestimate observed MAGT across the TP (Bias = $-0.77^{\circ}C$), which could
 321 be attributed to inaccuracies of forcing, soil stratigraphy dataset, and imitated processes
 322 representation (Langer et al., 2024) and setting for the maximum snow height (0.1m).
 323 Overall, our model displayed the ability to reproduce the MAGT in the TP permafrost

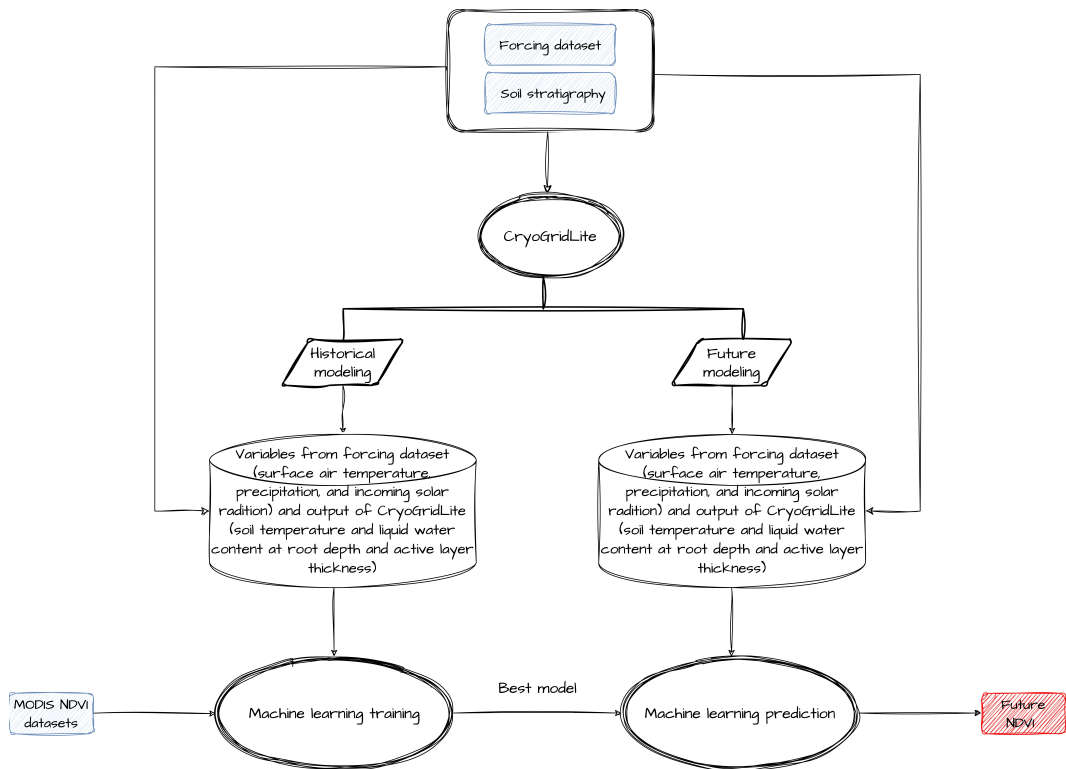


Figure 2. Flowchart of the process used to estimate the future vegetation change

324 areas well. Compared with the model capability on the MAGT, there was a poorer re-
 325 lationship between simulated and observed ALT, with a Pearson correlation coefficient
 326 of 0.17 (Figure 3 (b)). Similarly, the model exhibited a trend of underestimating the mea-
 327 sured ALT compared to the observed values (Bias = -0.03 m), which aligns with the sim-
 328 ulated cold bias for MAGT. The deviations between measured and modeled ALT were
 329 likely to be explained by inadequate forcing and soil dataset, shortcomings of the model
 330 (Langer et al., 2024), the cooling effect of shallow snow cover (0.1m), and high spatial
 331 heterogeneity of ALT on the TP (B. Cao et al., 2017; Ni et al., 2021). Nevertheless, our
 332 model reproduced the observed ALT on the TP, with modeled ALT deviations of $\pm 1\text{ m}$
 333 for most sites (59.1%). A more detailed model evaluation was conducted for the soil tem-
 334 perature at upper soil depth across the TP due to the soil temperature at the root zone
 335 as an input index in machine learning (see Supporting Information Table S4 and Fig-
 336 ure S3). In this research, CryoGridLite, driven by CMFD data, was employed to model
 337 the distribution of permafrost across the TP during the historical period (Figure 3 (c)).
 338 To demonstrate the capability of CryoGridLite to reproduce spatial permafrost occur-
 339 rence, we juxtaposed our simulation results with five contemporary maps of permafrost
 340 distribution based on different approaches, thereby providing a comprehensive compar-
 341 ison and validation of our modeling results (Zou et al. (2017); Ran et al. (2018); Obu et
 342 al. (2019); Ni et al. (2021); Z. Cao et al. (2023); Figure 3 (d-h)). The comparison largely
 343 confirmed that the projected area of permafrost was consistent between our results and
 344 those of previous studies. Our modeling results indicated that the most likely permafrost
 345 areas on the TP were $1.10 \times 10^6 \text{ km}^2$ for the period 2000–2018 (excluding lakes and glaciers),
 346 which agreed well with other five studies ($1.04\text{--}1.28 \times 10^6 \text{ km}^2$). However, local differ-
 347 ences were found between our results and other permafrost maps, which were most pro-
 348 nounced in the southern TP and along the southeast margin of the zone of continuous
 349 permafrost. It can be explained in several parts, first, spatial resolution and study pe-

350 riod differences; lower resolutions (i.e., 0.1°) make it difficult to capture the dynamics
 351 of permafrost changes at the boundaries of permafrost zones (Ni et al., 2021) and study
 352 period leads a slight discrepancy for the modeled results. Second, simulated approach
 353 differences; our results offer a dynamic, transient modeling perspective. In contrast, other
 354 models, such as the temperature at the top of the permafrost model and the surface frost
 355 number model, while simpler and requiring less data input, are not as equipped to cap-
 356 ture transient effects or to project the evolution of permafrost accurately (Smith et al.,
 357 2022). Besides, the permafrost-modeled results of the machine learning model have data
 358 dependence and the risk of overfitting (Ni et al., 2021). Third, the definition of permafrost
 359 differences; we diagnose the absence or presence of permafrost relying on the MAGT at
 360 the zero depth of annual amplitude. Other studies adopt different criteria to determine
 361 the permafrost exists (e.g., the MAGT at the top of permafrost or the 10 m depth). In
 362 summary, despite limitations our model provides a reasonable basis for describing spa-
 363 tially and temporally transient conditions of permafrost on the TP as input variable for
 364 the following analysis.

3.1.2 Machine learning model

We utilized the pre-partitioned test dataset to evaluate the performance of two machine-learning algorithms in modeling the NDVI_{GS} over the permafrost and non-permafrost areas of the TP (Figure 4). A comparison analysis of the two results (Figure 4 (a-b)) revealed that each algorithm proficiently captured the satellite-derived NDVI_{GS} values on the permafrost areas. The performance metrics (with R² >= 0.65, BIAS <= 0.01, RMSE <= 0.08, and KGE >= 0.59) suggested each model demonstrated robust capabilities in capturing the NDVI_{GS} dynamics over the permafrost regions of the TP. In comparison, the LightGBM model has better performance. Consequently, we selected the lightGBM model for further analysis of the spatial and temporal variability of NDVI_{GS} and its underlying drivers under different future climate scenarios. Additionally, complimentary assessments conducted for NDVI_{GS} over the non-permafrost areas underscored the simulation ability of both algorithms were remarkably similar and both can well repeat the changes in NDVI_{GS} (Figure 4 (c-d)).

3.2 Spatial and temporal patterns of the permafrost dynamics on the TP

To elucidate the spatiotemporal dynamics of permafrost variability on the TP throughout this century, we executed four distinct simulations driven by the AWI-CM-1-1-MR (Figure 5) and MPI-ESM1-2-HR (Supporting Information Figure S4) models, under both the SSP1-2.6 and SSP5-8.5 scenarios. Our findings revealed that spatial variability of permafrost distribution under the AWI-CM-1-1-MR, particularly by mid-century (2041–2060), manifested as a moderate reduction relative to the baseline period (2000–2018). This reduction was predominantly observed along the northern boundary of the continuous permafrost zone, southern regions of the TP, and the Three Rivers Sources (TRS) region (the red box in Figure 1 (a)), with negligible disparities between the lower and higher emission pathways (Figure 5 (a, c, e, g)). In contrast, by the end of the century (2081–2100), the majority of the permafrost areas were projected to remain relatively intact under SSP1-2.6, while areas that experienced permafrost thaw by mid-century continued to show visible degradation (Figure 5 (b, f)). Under a scenario of intensified climate warming, substantial thawing of existing permafrost was anticipated, particularly in the southwestern and southern parts of the TP, where the MAGT at the depth of zero annual amplitude was likely to approach or even exceed 0°C (Figure 5 (d, h)). The TRS region, in particular, was expected to undergo extensive permafrost degradation. Conversely, the northwestern areas of the Changtang Plateau and the Qilian Mountains were projected to maintain their permafrost coverage (Figure 5 (d, h)). In examining the projected changes in MAGT under the AWI-CM-1-1-MR, significant spatial heterogeneity

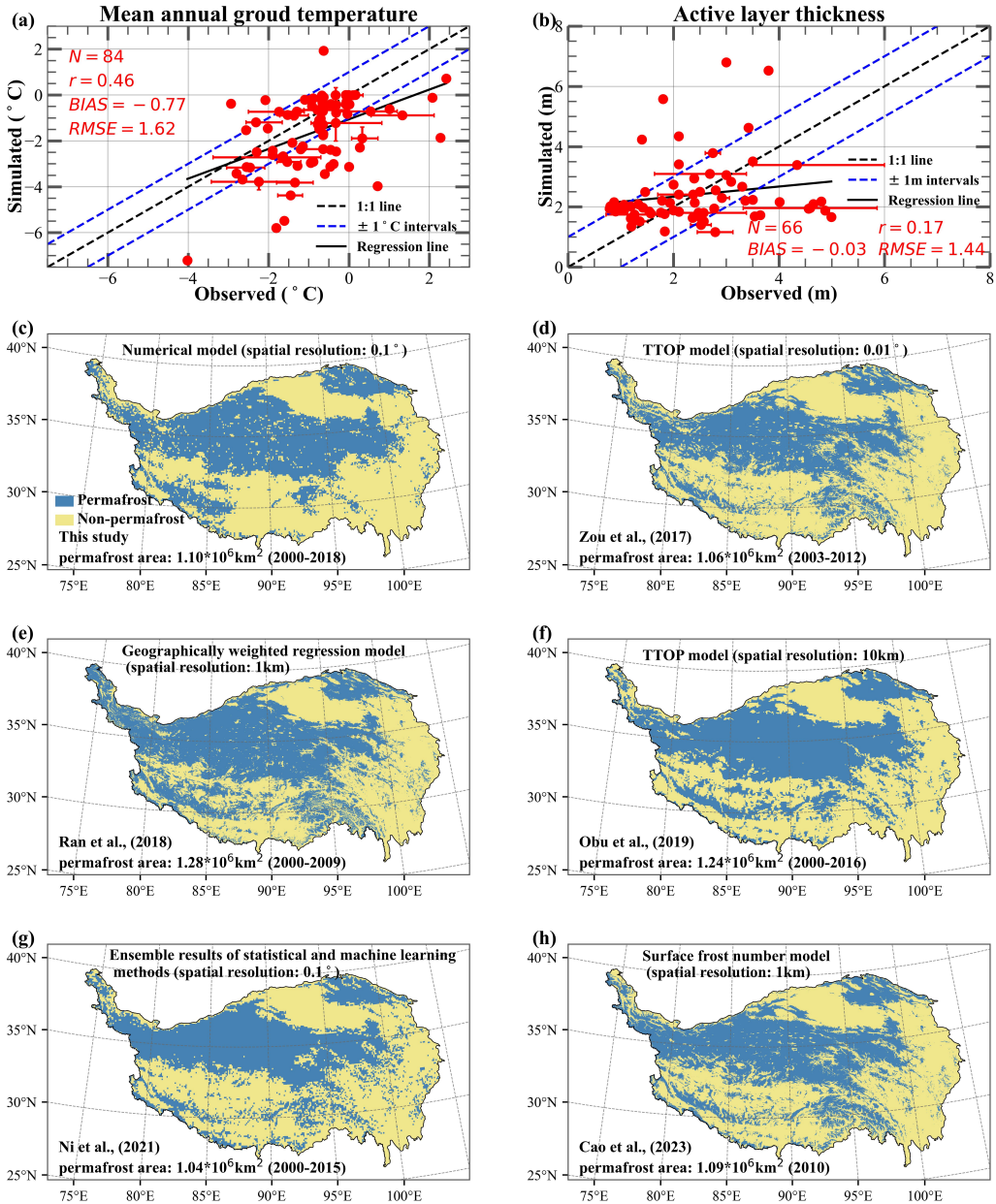


Figure 3. (a) Scatter plot illustrates the comparison results between the observed and simulated mean annual ground temperature (MAGT) for 151 records located within 84 different grid cells. (b) Scatter plot compares the observed and modeled active layer thickness (ALT) for 86 records located within 66 different grid cells. (c) Spatial distribution of permafrost during 2000–2018 over the Tibetan Plateau based on CryoGridLite model. (d-h) Spatial distribution of permafrost on the Tibetan Plateau from other studies. In (a) and (b), each point indicates the average value of observed and modeled MAGT/ALT in the same grid cell. The horizontal error bars represent the range of all observed MAGT/ALT located in the same grid cell, and vertical error bars indicate the range of simulated MAGT/ALT in the same grid cell.

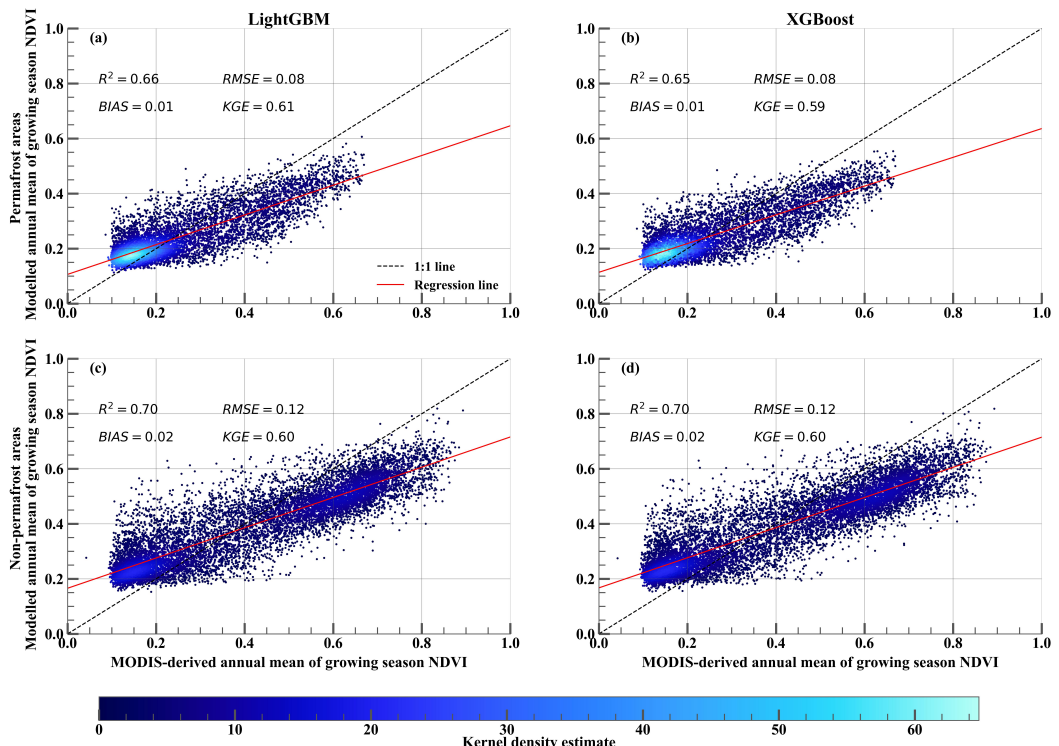


Figure 4. Density scatter plot for comparison between observed and modeled mean annual $NDVI_{GS}$ in the permafrost and non-permafrost areas from 2015 to 2018. (a, c) LightGBM, (b, d) XGBoost. The black dashed line indicates a 1:1 line. The red line represents the regression line.

401 was observed across the permafrost regions. Under the SSP1–2.6 scenarios, this variability
 402 contrasted with the SSP5–8.5 scenarios; specifically, the eastern permafrost regions
 403 were trending warmer, whereas the central Changtang Plateau and the Pamir Mountains
 404 experiencing cooling trends (Figure 5 (a-b)). The future dynamics of MAGT in these
 405 permafrost areas were expected to be largely influenced by the extent of climatic warming
 406 (Figure 5 (c-d)). Figure 5 (e-h) depicts the changes in ALT across the permafrost
 407 areas on the TP under the AWI-CM-1-1-MR for both mid-century and end-century, un-
 408 der two contrasting scenarios, relative to the 2000–2018 baseline period. The pattern of
 409 ALT changes mirrored that of MAGT, with a notable increase in ALT observed in the
 410 TRS region and along the Qinghai-Tibet Engineering Corridor (QTEC), throughout the
 411 century under both scenarios. Therefore, additional actions are needed to maintain the
 412 stability of infrastructure in the QTEC in the future. However, in the western TP, the
 413 evolutionary trajectory of ALT was contingent upon the extent of climate warming, i.e.
 414 ALT was likely to decrease under stable climatic conditions, while it tended to increase
 415 in scenarios of ongoing climate warming. The spatial distribution of MAGT, ALT, and
 416 permafrost areas under both scenarios under the MPI-ESM1-2-HR was in correspondence
 417 with the results from AWI-CM-1-1-MR (Supporting Information Figure S4).

418 We further detected the time evolution of permafrost areas, MAGT, and ALT across
 419 the TP from 2019 to 2100 under SSP1–2.6 and SSP5–8.5 scenarios (Figure 5 (i-k)). The
 420 projected permafrost area consistently showed a decreasing trend across different climate
 421 scenarios; however, the rate of this decline varied. Permafrost areas decreased gradually
 422 from $1.06 \pm 0.00 \times 10^6 \text{ km}^2$ (mean \pm standard deviation) to $0.87 \pm 0.04 \times 10^6 \text{ km}^2$ under
 423 SSP1-2.6 and $0.49 \pm 0.02 \times 10^6 \text{ km}^2$ under SSP5-8.5 during 2019–2100 at a rate of $-0.02 \pm 0.00 \times 10^6 \text{ km}^2$
 424 per decade (SSP1-2.6) and $-0.07 \pm 0.00 \times 10^6 \text{ km}^2$ per decade (SSP5-8.5) under the lower
 425 and higher emission pathway, respectively (Figure 5 (i)). By 2100, the permafrost ar-
 426 eas, under SSP1-2.6 and SSP5-8.5, were projected to decrease by $22 \pm 3\%$ and $56 \pm 2\%$,
 427 respectively, compared to the baseline period.

428 Figure 5 (j) presents the changes in MAGT during the period 2019–2100. Although
 429 projected MAGT based on AWI-CM-1-1-MR and MPI-ESM1-2-HR varies considerably
 430 under SSP1–2.6, MAGT increases slightly in the first half-century and decreases further
 431 until the end of the century, with insignificant changes in MAGT throughout the cen-
 432 tury. Under SSP5–8.5 scenarios, MAGT increased significantly to around -1.0°C by 2100.
 433 Relative to the mean MAGT ($-2.26 \pm 0.17^\circ \text{C}$) in the baseline period, MAGT decreased
 434 by about $-0.07 \pm 0.18^\circ \text{C}$ and $-0.26 \pm 0.15^\circ \text{C}$ under SSP1–2.6 by mid-century (2041–2060)
 435 and end-century (2081–2100), respectively, while, under SSP5–8.5, MAGT increases by
 436 about $0.28 \pm 0.03^\circ \text{C}$ and $1.20 \pm 0.05^\circ \text{C}$ by the period 2041–2060 and 2081–2100, respec-
 437 tively.

438 The time series of simulated ALT in the permafrost areas are shown in Figure 5
 439 (k). The temporal variation of ALT was different in both climate scenarios. Under the
 440 lower emission pathway, ALT had no evident change throughout this century, while in-
 441 creasing to around 5.0 m by 2100 under severe climate warming. By the middle of this
 442 century, ALT in the permafrost areas of the TP increased by approximately $0.03 \pm 0.17 \text{ m}$
 443 to $0.37 \pm 0.07 \text{ m}$ under SSP1–2.6 and SSP5–8.5 scenarios, respectively. However, ALT
 444 decreased by about $0.24 \pm 0.11 \text{ m}$ under SSP1–2.6 and increased by about $1.87 \pm 0.14 \text{ m}$
 445 under SSP5–8.5 by the end of this century.

446 3.3 Spatial and temporal patterns of the vegetation in the permafrost 447 areas on the TP

448 Analysis of satellite imagery data at the grid cell level (i.e. 0.1°) revealed that, dur-
 449 ing the period from 2000 to 2018, NDVI_{GS} trends in the majority of permafrost areas
 450 (67.17%) on the TP did not exhibit significant changes ($p\text{-value} > 0.05$). A portion of
 451 the permafrost areas, constituting 31.55%, displayed an increase in NDVI_{GS} ($p\text{-value} <$

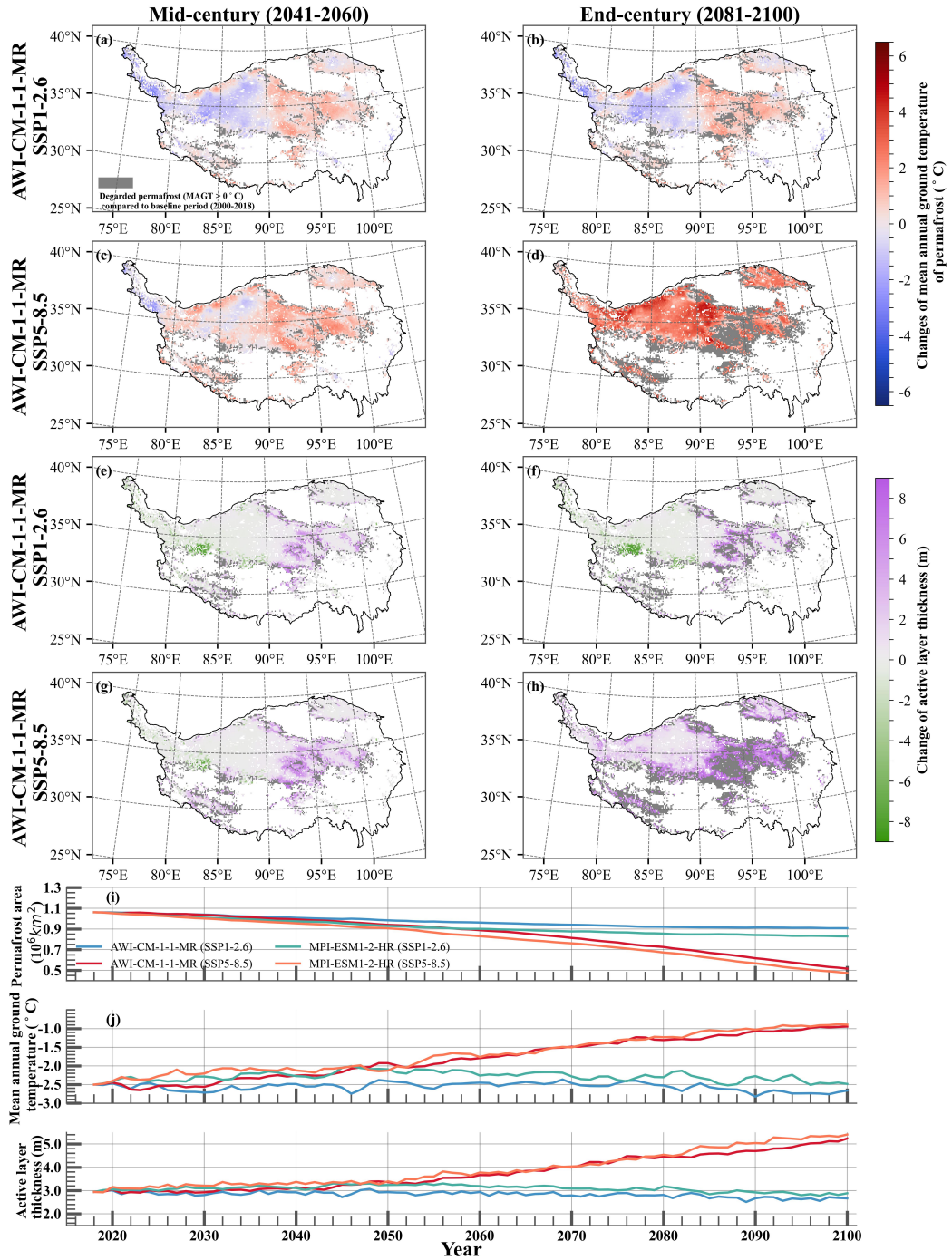


Figure 5. Spatial changes of the mean annual ground temperature (a-d) and active layer thickness (e-h) on the Tibetan Plateau by mid-century (2041–2060) and end-century(2081–2100) under SSP1–2.6 and SSP5–8.5 scenarios from AWI-CM-1-1-MR, related to the baseline period (2000–2018), respectively. (i-k) Time evolution of the changes in permafrost areas, mean annual ground temperature, and active layer thickness from 2019 to 2100 under the SSP1-2.6 and SSP5-8.5 scenarios. The grey area indicates degraded permafrost areas compared with the baseline by the mid-century (2041–2060) and end-century (2081–2100), and the blue, red, green, and orange lines represent the SSP1-2.6 and SSP5-8.5 scenarios from AWI-CM-1-1-MR and SSP1-2.6 and SSP5-8.5 scenarios from MPI-ESM1-2-HR, respectively.

452 0.05), whereas a minimal area, representing only 1.28% experienced a decline in NDVI_{GS}
 453 ($p\text{-value} < 0.05$) (Figure 6 (c)). Within the non-permafrost areas, 18.96% and 2.24% proportion
 454 of the area experienced an increased and decreased NDVI_{GS} , respectively, during the same period (Figure 6 (d)). Although we utilized data from both permafrost and
 455 non-permafrost areas across all grid cells to construct our training dataset, the predic-
 456 tive accuracy for extrapolations beyond the training data range was notably constrained,
 457 especially under the high-emission SSP5–8.5 scenarios, due to the inherent data depen-
 458 dency in machine learning. To enhance the robustness of our future NDVI change sim-
 459 ulations, we narrowed down our predictions to 2050. Our machine learning analysis, based
 460 on the SSP1–2.6 scenarios using two ESMs, indicated a stable NDVI_{GS} (ensemble mean)
 461 across the permafrost areas, with no significant alterations anticipated from 2019 through
 462 2050 ($p\text{-value} > 0.05$), maintaining an average NDVI_{GS} of 0.25 ± 0.03 (Figure 6 (a); blue
 463 and green line). Spatial distribution analysis of the mean annual NDVI_{GS} trend under
 464 both ESMs showed no considerable shifts in vegetation conditions over 85–97% of the
 465 permafrost regions up to the middle of the century (Figure 6 (e) and Supporting Infor-
 466 mation Figure S5 (a)), this stability likely attributable to the relatively stable climatic
 467 conditions associated with lower emission trajectories. In contrast, under the SSP5–8.5
 468 scenarios, results from the Mann-Kendall test suggested a marginally increasing trend
 469 in the ensemble mean of the NDVI_{GS} anomaly time series ($0.05 < p\text{-value} < 0.10$), with
 470 a rate of 0.01 ± 0.00 per decade (Figure 6 (a); orange and red line). Moreover, over 7–
 471 29% of the permafrost areas exhibited increased NDVI_{GS} , while a significant decrease
 472 in NDVI_{GS} was observed in only about 0.33–1.17% of the area under both scenarios (Fig-
 473 ure 6 (g) and Supporting Information Figure S5 (c)). Consequently, our findings hint at
 474 a potential slightly increased NDVI_{GS} within the permafrost areas over the TP, amidst
 475 the ongoing severe climate warming projected by the middle of the century. Figure 6 (b,
 476 f, h) and Supporting Information Figure S5 (b, d) outline the time series of the NDVI_{GS}
 477 anomaly and spatial distribution of the mean annual NDVI_{GS} trend across the non-permafrost
 478 areas. From 2019 to 2050, the ensemble mean of the time series for mean annual NDVI_{GS}
 479 anomaly in the majority of non-permafrost areas was expected to remain relatively sta-
 480 ble under SSP1–2.6 scenarios ($p\text{-value} > 0.05$), while a slight increase in NDVI_{GS} trend,
 481 similar with the permafrost areas, is anticipated under SSP5–8.5 scenarios ($0.05 < p\text{-}
 482 value} < 0.10$). Spatially, 1.90–5.03% permafrost and 6.10–8.77% non-permafrost areas
 483 showed an increasing trend under the SSP1–2.6 and SSP5–8.5 scenarios, respectively. In
 484 summary, NDVI_{GS} trends in most permafrost and non-permafrost areas were expected
 485 to remain stable under lower emission pathways till the midpoint of this century. Con-
 486 versely, under higher emission pathways, NDVI_{GS} was likely to exhibit an increasing trend
 487 in permafrost and non-permafrost areas. According to the vegetation types dataset of
 488 the TP Zhou et al. (2022), the alpine meadow and alpine steppe constituted the primary
 489 vegetation in the permafrost areas. We further detected the annual NDVI_{GS} change for
 490 different vegetation types (alpine steppe and alpine meadow) in the permafrost areas (Sup-
 491 porting Information Figure S6). Our results showed that areas with increased mean an-
 492 nual NDVI_{GS} outnumbered those with decreased mean annual NDVI_{GS} for both veg-
 493 etation types, although the extent of this disparity varied under the two scenarios.
 494

495 3.4 Important features of spatiotemporal variability of the vegetation 496 in the permafrost areas on the TP

497 The evolution of vegetation is influenced by an interplay of various climatic and
 498 terrestrial factors (Hawinkel et al., 2016; Y. Wei et al., 2022; Higgins et al., 2023). We
 499 performed ridge regression for both permafrost and non-permafrost areas to identify the
 500 absolute values of the contribution of each explanatory factor and detect the most im-
 501 portant variables to NDVI_{GS} change. For the baseline period, climate variables (i.e. SAT_{GS} ,
 502 PRE_{GS} , and SIN_{GS}) contributed notably (59.34% of permafrost areas and 68.65% of non-
 503 permafrost areas) to the NDVI_{GS} change, specifically, the contribution of SAT_{GS} was
 504 the largest (22.99%) in the permafrost and was the secondary important factor (21.53%)

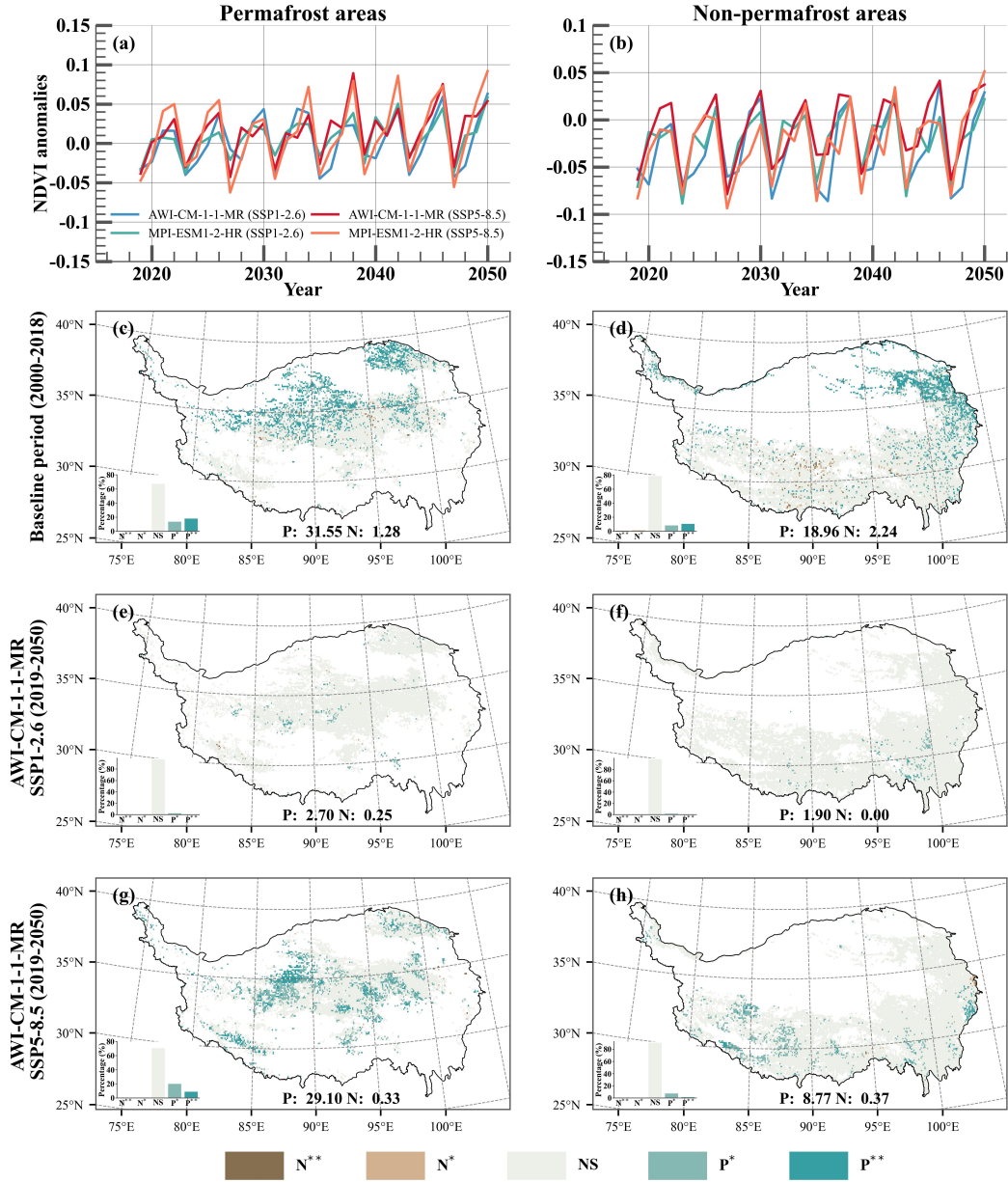


Figure 6. (a-b) Time series of mean annual NDVI_{GS} anomalies (minus the mean value during 2000–2018) from 2019 to 2050 under the future climate conditions on the permafrost and non-permafrost areas over the TP. The blue, red, green, and orange lines represent SSP1–2.6 and SSP5–8.5 scenarios from AWI-CM-1-1-MR and MPI-ESM1-2-HR, respectively. (c-h) Spatial patterns of mean annual NDVI_{GS} trend across the permafrost and non-permafrost areas during the baseline (2000–2018) and future periods (2019–2050) under different climate scenarios from AWI-CM-1-1-MR. N, NS, and P indicate negative, non-significant, and positive trends. * and ** represent significance at p-value < 0.05 and 0.01, respectively

in the non-permafrost area of the plateau, the PRE_{GS} was identified as the third important factor and made similar contributions (17.52% and 19.67%) in the permafrost and non-permafrost areas, the SIN_{GS} had more contributions to the NDVI_{GS} change in the non-permafrost areas (27.45%) than that of in the permafrost areas (18.84%) (Figure 7 (a-d)). For the terrestrial variables (i.e. ST_{GS}, LWC_{GS}, and ALT_{GS} [excluded in non-permafrost areas]), they contributed to the NDVI_{GS} change of approximately 40% of the permafrost areas and 30% of the non-permafrost areas. We used the same method to examine the dominant factors controlling the change of annual NDVI_{GS} during 2019–2050 under different climate scenarios and different ESMs (Figure 7 (e-l) and Supporting Information Figure S7 (a-h)). The results revealed that predominant factors affecting the future NDVI_{GS} changes in permafrost and non-permafrost areas under the different scenarios remained largely consistent. That is, under the SSP1–2.6 and SSP5–8.5 scenarios, it was found that SAT_{GS} and LWC_{GS} emerged as the primary determinants of the interannual variability in NDVI_{GS} across permafrost areas, influencing between 61.24% and 76.26% of these areas. In non-permafrost areas on the TP, SIN_{GS} was identified as the predominant driver behind NDVI_{GS} interannual variability, affecting 33.38% to 45.59% of the areas under both scenarios. Supporting Information Figure S8 depicts the spatial patterns and relative importance of each explanatory variable across diverse vegetation types. The NDVI_{GS} interannual variation in both vegetation types was responsive to variations of climatic factors in the baseline period (approximately 60%). Aiming at the future periods, SAT_{GS} and LWC_{GS} explained a much larger portion of the NDVI_{GS} variations than other factors in both vegetation types (Supporting Information Figure S8 (e-l)). Overall, the interannual variability of the NDVI_{GS} tended to be predominantly controlled by the climate variables in both permafrost and non-permafrost areas from 2000 to 2018. Compared to the baseline period, our study indicated that SAT_{GS}, LWC_{GS} and SIN_{GS} were the main contributors to the NDVI_{GS} change in the permafrost and non-permafrost areas in the future periods (Figure 7 (e-l), Supporting Information Figure S7 (a-h)). Consequently, surface air temperature, liquid water content at the root zone, and incoming solar radiation played an important role in future NDVI_{GS} evolution on the TP.

4 Discussion

4.1 Comparison with previous modeling studies of the permafrost state and vegetation conditions on the TP

In this study, we utilized a computationally efficient numerical permafrost model (CryoGridLite) driven by climatic forcing data to simulate the thermal state of permafrost and ALT over the TP from 1979 to 2100. Table S5 summarizes the simulation results of the thermal state of permafrost and ALT on the TP under present and future climate conditions in the past 10 years based on different approaches. For the historical period, our results fell within the range of these studies for the permafrost state (MAGT: [-3.32° C, -1.35° C]; Permafrost areas: [1.01 × 10⁶ km², 1.66 × 10⁶ km²]) and ALT [1.24m, 3.23m]. As previously mentioned, the differences among these simulation results can be attributed to spatial resolution and study period, study approaches, and the definition of the permafrost state and ALT, etc. For the future period, although there were variations in magnitude and trends for the permafrost state and ALT between our study and others, all demonstrated that permafrost degradation over the TP would be an inevitable consequence in the 21st century under the SSP5–8.5/Representative Concentration Pathway (RCP) 8.5 scenarios. Meanwhile, under the SSP1–2.6/RCP2.6 scenarios, permafrost was anticipated to exhibit relative stability or only slight warming until the end of the century and was most likely aggradation in the northwest of the plateau due to the cooling surface air temperature under the SSP1–2.6 scenarios. In addition to the reasons mentioned above, the divergence in projections could largely be explained by the disparities among the ESMs employed in these studies. For instance, G. Zhang et al. (2022) used

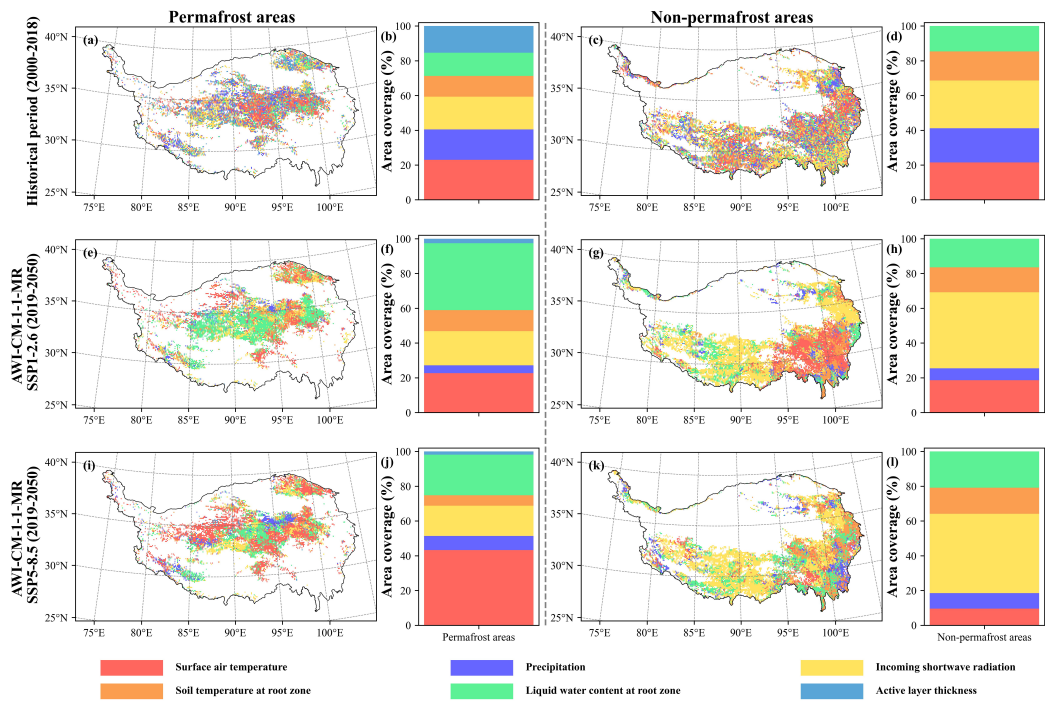


Figure 7. Spatial distribution of the dominant factors to the $NDVI_{GS}$ changes over different periods in the permafrost and non-permafrost areas. (a, c) Baseline period (2000–2018). (e, g) Future period (SSP1–2.6; AWI-CM-1-1-MR). (i,k) Future period (SSP5–8.5; AWI-CM-1-1-MR). The barplot (b, d, f, h, j, l) represents the proportion of the contribution of each variable in the permafrost and non-permafrost areas under AWI-CM-1-1-MR.

557 the Noah-LSM driven by five ESMs to project permafrost stability on the TP through-
 558 out this century. Their findings revealed significant variances among the ESMs' projec-
 559 tions under identical scenarios (e.g. under the SSP5-8.5 scenarios, simulations driven by
 560 CESM2 and EC-Earth3 suggested that permafrost was highly likely to vanish by 2100,
 561 while, projections based on MPI-ESM1-2-HR (also used in our study) indicated that ap-
 562 proximately $0.5 \times 10^6 km^2$ (similar with our results) of permafrost might persist by the
 563 end of the century).

564 To project the NDVI in the future on the TP, we employed statistical models trained
 565 by machine-learning algorithms under two contrasting climate scenarios in this study.
 566 For the historical period (2000–2018), MODIS imagery indicated that the $NDVI_{GS}$ showed
 567 an increasing trend over the TP, with a rate of 0.01 per decade, and 24% proportion of
 568 the area covered by plants exhibits greening (Supporting Information Figure S2 (a-c)).
 569 In addition to the MODIS NDVI data, other ecological indicators (e.g. LAI, NPP, EVI,
 570 fractional vegetation coverage [FVC]) demonstrated that vegetation greenness increased
 571 on the TP since 2000 (Piao et al., 2020; M. Shen et al., 2022; Yang et al., 2023; X. Zhang
 572 & Li, 2023). Regarding vegetation evolution in the future, although few studies have elu-
 573 cidated the magnitude and trends of NDVI in the permafrost areas on the TP (H. Li et
 574 al., 2024), studies based on other vegetation factors and methods showed that under the
 575 background of future climate change, there was a potential for vegetation greening on
 576 the TP (Q. Gao et al., 2016; Mahowald et al., 2016; W. Liu et al., 2020; Cuo et al., 2022;
 577 M. Shen et al., 2022; Kong et al., 2023), which aligns with our study. For example, Q. Gao
 578 et al. (2016) and Cuo et al. (2022) applied the Lund-Potsdam-Jena dynamic global veg-
 579 etation model (LPJ-DGVM) to quantify the annual NPP changes on the TP under CMIP5/CMIP6
 580 scenarios. Their findings indicated a general increase in annual NPP, with a notable shift
 581 in the dominant vegetation, as alpine shrubs are projected to replace alpine meadows
 582 and steppes. The simulation results from ESMs (CMIP5) and regional climate models
 583 indicated a continued increasing trend of LAI by the end of the century in the north-
 584 ern temperate region (25–50° N: including the TP) and TP (Mahowald et al., 2016; W. Liu
 585 et al., 2020). Kong et al. (2023) constructed a framework of machine learning algorithms
 586 to predict the evolution trajectory of FVC in China under four SSP scenarios from 2019
 587 to 2060, with FVC showing an increasing trend except for the east region of China. H. Li
 588 et al. (2024) indicated that under the various climate scenarios, along with significant
 589 permafrost degradation, the TP exhibited a greening (NDVI) trend in vegetation which
 590 persists until the end of the century. In addition to employing the vegetation indices to
 591 analyze future vegetation greenness, a recent review summarized the potential plant phe-
 592 nology changes on the TP in this century, which included the advanced start of the grow-
 593 ing season and the delayed end of the growing season, causing vegetation greening on
 594 the TP (M. Shen et al., 2022). Besides, we would like to point out that there are ongo-
 595 ing debates regarding the continued vegetation greening phenomenon that occurs on the
 596 TP and the prospect of the TP becoming a net carbon sink in the future, especially con-
 597 sidering carbon released by thawing permafrost and enhanced soil and plant respiration
 598 (X. Jin et al., 2021; D. Wei et al., 2021; Ehlers et al., 2022; T. Wang et al., 2022). Con-
 599 sequently, an enhanced focus on the vegetation conditions within the permafrost regions
 600 of the Tibetan Plateau is warranted in future studies.

601 4.2 Important features of vegetation greening

602 In our study, we used ridge regression to discern the absolute values of the contribu-
 603 tions of the driving factors for the NDVI changes on the TP. For the baseline period,
 604 the climatic variables were the important features of $NDVI_{GS}$ on the TP in both per-
 605 ma frost (approximately 60%) and non-permafrost areas (approximately 70%) (Figure
 606 7, Supporting Information Figure S7). Piao et al. (2020) noted that dynamic global veg-
 607 etation models suggested that CO₂ fertilization (a phenomenon widely acknowledged for
 608 enhancing vegetation growth) continued to be the predominant factor driving vegeta-
 609 tive greening on a global scale. However, in northern high latitudes and the TP, it is the

increasing temperatures that primarily contributed to the observed greening trends (LAI). Statistical analysis (Teng et al., 2021; X. Li et al., 2022; M. Shen et al., 2022; T. Wang et al., 2022) and sensitivity experiments (Y. Wang et al., 2023) also demonstrated that climate change played an important role in vegetation growth over the past 40 years on the TP, albeit with contributions of varying magnitudes. This variability in quantitative contributions was attributed to the differential impact of various input explanatory variables (e.g. climate variables, terrain, soil properties) and different data sources (e.g. MODIS data, Global Inventory Modeling and Mapping Studies NDVI product [GIMMS NDVI], and SPOT VEGETATION imagery [SPOT-VEG NDVI]). For the future period, our findings indicated that, compared with the baseline period, $NDVI_{GS}$ showed a potential increasing trend likely occurring in the permafrost areas under the SSP5–8.5 scenarios, mainly attributed to the change of SAT_{GS} and LWC_{GS} . Supporting Information Figure S9 and S10 indicate the spatiotemporal distribution of LWC_{GS} and SAT_{GS} in the permafrost areas from 2019 to 2050. In the vast majority of permafrost regions, both the SAT_{GS} and the LWC_{GS} have exhibited an increasing trend. This was in agreement with the results from J. Gao et al. (2017), who combined the LPJ-DGVM with the geographical regression, and R. Cao et al. (2023), who conducted multiple sensitivity experiments based on machine learning algorithms. All indicated that temperature would more significantly affect vegetation changes over the TP. One potential explanation is that warmer temperatures extend the duration of growing seasons, enhance photosynthetic activity, and lead to greater biomass accumulation ((J. Gao et al., 2017; X. Li et al., 2022; M. Shen et al., 2022)). Additionally, our results emphasized the important role of LWC_{GS} in vegetation growing in the permafrost areas. Besides, it is important to acknowledge that in this study we only considered the impact of a few variables on $NDVI_{GS}$ change over the TP, without taking into account other factors. Future studies should synthesize more driving factors and implement more analysis methods (e.g. partial correlation analysis or structural equation model) to improve our understanding of the vegetation change on the TP.

4.3 Model limitation and uncertainty

While the CryoGridLite model capably replicates the mean state (Figure 3 (a-b), Table S4) and temporal evolution (Supporting Information Figure S3) of the permafrost thermal regime across the TP, there is a need for further development and enhancements to diminish the uncertainty of simulations. For instance, the single offline simulation driven by singular meteorological forcing data (He et al., 2020) and soil stratigraphy datasets (Y. Dai, Xin, et al., 2019; Y. Dai, Wei, et al., 2019) and a fixed maximum snow depth (i.e., 0.1 m) and snow density (i.e., 150 kg m^{-3}) for all grid cells may introduce a large degree of uncertainty for simulation (W. Wang et al., 2016; Lu et al., 2020; Langer et al., 2024). Hence, conducting ensemble parameter simulations (including forcing, soil, and snow properties datasets) should be the direction of our subsequent research endeavors (Nitzbon et al., 2023; Langer et al., 2024). This approach is crucial for a more accurate quantification of the permafrost thermal state across the TP. Furthermore, compared with Nitzbon et al. (2023) and Langer et al. (2024), in this tailored version of CryoGridLite, we implemented the surface energy balance (Supporting Information Text S1.1) and "bucket" scheme (Supporting Information Text S1.2) to calculate the dynamics of upper boundary conditions and groundwater changes, respectively. However, as pointed out by Langer et al. (2024), the model calculated the ground freezing by an enthalpy–temperature relation of free water instead of accurate soil freezing characteristic curves, and the model does not account for the interactions between permafrost and vegetation (Stuenzi, Boike, Cable, et al., 2021; Stuenzi, Boike, Gädeke, et al., 2021), subsidence processes following excess ice melting (Nitzbon et al., 2019), and sub-grid lateral fluxes (Nitzbon et al., 2021), which are known to affect permafrost thaw trajectories in complex landscapes. Further detailed descriptions of model limitation and uncertainty can be found in Langer et al. (2024). Moreover, for future permafrost simulations, we employed two ESMs (AWI-CM-

663 1-1-MR and MPI-ESM1-2-HR) to drive our CryoGridLite model. These ESMs have demon-
 664 strated their capability in accurately reproducing mean annual and seasonal surface air
 665 temperatures over recent decades (R. Chen, Li, et al., 2022). However, significant dis-
 666 crepancies were observed in their representation of precipitation changes (R. Chen, Duan,
 667 et al., 2022), introducing a notable degree of uncertainty into our permafrost projections.
 668 This is due to the permafrost's thermal state being highly sensitive not only to air tem-
 669 perature but also to precipitation; increased rainfall can significantly mitigate permafrost
 670 degradation on the Tibetan Plateau (TP) (G. Zhang et al., 2021; Hamm et al., 2023).
 671 Therefore, to enhance our understanding of permafrost evolution on the TP, it is imper-
 672 ative to conduct additional simulations using a variety of ESMs

673 Regarding the NDVI changes predicted by our model, we acknowledge a certain
 674 degree of uncertainty inherent in the outputs of our machine learning algorithms. Pri-
 675 marily, these models are challenged by their reliance on data-driven approaches, which
 676 may lack a solid physical basis, transparency, interpretability, and a heightened sensi-
 677 tivity to outliers, potentially leading to instability or inaccurate predictions (G. Zhang
 678 et al., 2022; C. Shen et al., 2023). Therefore, in our study, although we implemented sev-
 679 eral strategies to overcome the inherent shortcomings of machine learning algorithms,
 680 to make our results more robust, we extrapolated the predicted NDVI only to 2050. In
 681 addition, while NDVI data are extensively utilized for assessing the vegetative state of
 682 the TP (Teng et al., 2021; T. Wang et al., 2022; Yang et al., 2023), the reliability of this
 683 satellite-derived data is considerably impacted by factors such as sensor characteristics,
 684 atmospheric interference, and soil background effects (Sha et al., 2020). Therefore, it is
 685 crucial for future research to incorporate a broad spectrum of vegetation indices (e.g. LAI,
 686 EVI, NPP, soil-adjusted vegetation index) and apply more data to feed machine learn-
 687 ing model to reduce these errors and enable a more comprehensive analysis of vegeta-
 688 tive dynamics on the TP, particularly against the backdrop of ongoing climatic warm-
 689 ing. Moreover, we would like to point out that $NDVI_{GS}$ predictions in this study were
 690 based on MODIS satellite imagery. Owing to the data dependency of the machine learn-
 691 ing model, the use of alternative NDVI products as response variables might yield di-
 692 vergent results. This is particularly evident in the study of Yang et al. (2023), which em-
 693 ployed multi-source data to investigate vegetation changes on the TP since 2000, reveal-
 694 ing significant spatiotemporal discrepancies among MODIS data, GIMMS NDVI, and
 695 SPOT-VEG NDVI (e.g. SPOT-VEG NDVI ($p < 0.001$) and MODIS NDVI ($p < 0.05$)
 696 indicated a significant increasing trend, while GIMMS NDVI data ($p < 0.534$) did not
 697 show a significant increasing trend in NDVI on the TP). Meanwhile, the selection of ex-
 698 planatory variables significantly influences the determination of the quantitative contri-
 699 butions of predominant factors. Additionally, vegetation browning events induced by abrupt
 700 permafrost thaw (Heijmans et al., 2022) and vegetation greening occurring in thermokarst-
 701 drained lake basins (Y. Chen et al., 2023) are not considered in our study, which play
 702 an important role in controlling vegetation growth. Despite several shortcomings in our
 703 permafrost model and machine learning algorithms, our results attempt to provide a frame-
 704 work for exploring future vegetation changes in cold regions and identified limitations
 705 give opportunities for future improvements in our modeling approach.

706 5 Conclusions

707 In this study, we combined a numerical permafrost model (CryoGridLite) with machine-
 708 learning algorithms to analyze the vegetation conditions in the permafrost areas over the
 709 TP under various climate scenarios. Our model simulations, when compared with ob-
 710 servational data, efficiently captured the spatiotemporal patterns of permafrost across
 711 the TP during the baseline period (2000–2018), and the machine learning algorithm ef-
 712 fectively reproduced the interannual $NDVI_{GS}$ for the testing period (2015–2018). Forced
 713 by different climate conditions, our CryoGridLite model projected a continual decline
 714 in the permafrost areas on the TP in response to future climate warming. Under the SSP1-

2.6 scenario, mean annual ground temperature and active layer thickness appeared stable on average, but with regionally different responses i.e mean annual ground temperature and active layer thickness tended to increase in the Three River Source region and Qinghai-Tibet Engineering Corridor and decrease in the northwest of TP. However, under the SSP5-8.5 scenarios, there was a notable increase in both mean annual ground temperature and active layer thickness. Remote sensing imagery from MODIS suggested that approximately 30% of the permafrost areas on the TP showed an increasing trend in $NDVI_{GS}$ over the baseline period. The results of machine learning indicated that under the low emission scenario (SSP1–2.6), no significant change in $NDVI_{GS}$ was expected for >85% permafrost areas in the future. In contrast, under the high emission scenario, an increasing trend in $NDVI_{GS}$ in the future in about 7.31–29.10% of the permafrost areas, with less than 2% of the area experiencing a significantly decreased NDVI. Analysis of the contributory factors revealed that climatic factors during the growing season were the primary influence on NDVI alterations within the permafrost areas for the baseline period (2000–2018). For the future periods (2019–2050), it was found that the surface air temperature and liquid water content at the root zone during the growing season were anticipated to play a crucial, undeniable role in the $NDVI_{GS}$ changes within the permafrost areas. Although our approach has not yet fully accounted for the processes affecting the thermal state of permafrost and vegetation growth on the TP, the coupling of process-based and data-driven models provides a potential and meaningful pathway for detecting future vegetation evolution on the plateau. Our future research will aim to address the limitations of our methodology and deliver more accurate predictions, thereby enhancing our understanding of the carbon budget of the TP.

Open Research Section

The China Meteorological Forcing Dataset is available at <https://data.tpdc.ac.cn/zh-hans/data/8028b944-daaa-4511-8769-965612652c49>. The AWI-CM-1-1-MR and MPI-ESM1-2-HR datasets are available at <https://esgf-data.dkrz.de/search/cmip6-dkrz/>. The Vegetation types data is available at <https://www.resdc.cn/data.aspx?DATAID=122>. The shapefile of the boundary of the Tibetan Plateau is available at <https://www.geodoi.ac.cn/WebCn/doi.aspx?Id=135>. The shape file of lakes on the Tibetan Plateau is available at <https://www.tpdc.ac.cn/zh-hans/data/da4ffc9a-91fb-4ae9-8da5-c57aa92c8d2b>. The shape file of the glacier on the Tibetan Plateau is available at <https://www.tpdc.ac.cn/zh-hans/data/f92a4346-a33f-497d-9470-2b357ccb4246>. The Global high-resolution dataset of soil hydraulic and thermal parameters dataset is available at <http://globalchange.bnu.edu.cn/research/soil15.jsp>. The Global watertable depth dataset is available at https://glowasis.deltares.nl/thredds/catalog/opendap/opendap/Equilibrium_Water_Table/catalog.html. The Terrestrial heat flow dataset is available at <https://doi.org/10.1029/2019GC008389>. The ERA5-Land dataset is available at <https://cds.climate.copernicus.eu/cdsapp#!/dataset/reanalysis-era5-land?tab=overview>. The MODIS NDVI (MOD13A2, Version 6.1) is available from Google Earth Engine at https://developers.google.com/earth-engine/datasets/catalog/MODIS_061_MOD13A2. The CryoGridLite model code, machine-learning algorithms, and ridge regression method used for the simulations and analysis in this work are archived on Zenodo (<https://doi.org/10.5281/zenodo.10928146>).

Acknowledgments

Rui Chen was supported by the China Scholarship Council (No. 201904910442). Simone M. Stuenzi was supported by the Bundesministerium für Bildung und Forschung (grant no. 03F0931A).

763 **References**

- 764 Baral, P., Allen, S., Steiner, J. F., Gurung, T. R., & McDowell, G. (2023). Climate
 765 change impacts and adaptation to permafrost change in high mountain asia:
 766 a comprehensive review. *Environmental Research Letters*, *18*, 093005. doi:
 767 <https://doi.org/10.1088/1748-9326/acf1b4>
- 768 Cao, B., Gruber, S., Zhang, T., Li, L., Peng, X., Wang, K., ... Guo, H. (2017). Spa-
 769 tial variability of active layer thickness detected by ground-penetrating radar
 770 in the qilian mountains, western china. *Journal of Geophysical Research: Earth*
 771 *Surface*, *122*, 574–591. doi: <https://doi.org/10.1002/2016JF004018>
- 772 Cao, R., Ling, X., Liu, L., Wang, W., Li, L., & Shen, M. (2023). Remotely sensed
 773 vegetation green-up onset date on the tibetan plateau: Simulations and fu-
 774 ture predictions. *IEEE Journal of Selected Topics in Applied Earth Obser-*
 775 *vations and Remote Sensing*, *16*, 8125–8134. doi: <https://doi.org/10.1109/JSTARS.2023.3310617>
- 776 Cao, Z., Nan, Z., Hu, J., Chen, Y., & Zhang, Y. (2023). A new 2010 permafrost dis-
 777 tribution map over the qinghai-tibet plateau based on subregion survey maps:
 778 a benchmark for regional permafrost modeling. *Earth System Science Data*,
 779 *15*, 3905–3930. doi: <https://doi.org/10.5194/essd-15-3905-2023>
- 780 Chang, X., Jin, H., Zhang, Y., He, R., Luo, D., Wang, Y., ... Zhang, Q. (2015).
 781 Thermal impacts of boreal forest vegetation on active layer and permafrost
 782 soils in northern da xing'anling (hinggan) mountains, northeast china. *Arctic,*
 783 *Antarctic, and Alpine Research*, *47*, 267–279. doi: <https://doi.org/10.1657/AAAR00C-14-016>
- 784 Chen, C., Peng, X., Frauenfeld, O. W., Chu, X., Chen, G., Huang, Y., ... Tian, W.
 785 (2024). Simulations and prediction of historical and future maximum freeze
 786 depth in the northern hemisphere. *Journal of Geophysical Research: Atmo-*
 787 *spheres*, *129*, e2023JD039420. doi: <https://doi.org/10.1029/2023JD039420>
- 788 Chen, F., Zhang, X., & Chen, Z. (2023). High-temperature exposure and land trans-
 789 actions in china. *Earth's Future*, *11*, e2022EF003008. doi: <https://doi.org/10.1029/2022EF003008>
- 790 Chen, H., Nan, Z., Zhao, L., Ding, Y., Chen, J., & Pang, Q. (2015). Noah mod-
 791 elling of the permafrost distribution and characteristics in the west kunlun
 792 area, qinghai-tibet plateau, china. *Permafrost and Periglacial Processes*, *26*,
 793 160–174. doi: <https://doi.org/10.1002/ppp.1841>
- 794 Chen, J., Zhao, L., Sheng, Y., Li, J., Wu, X., Du, E., ... Pang, Q. (2016). Some
 795 characteristics of permafrost and its distribution in the gaize area on the
 796 qinghai-tibet plateau, china. *Arctic, Antarctic, and Alpine Research*, *48*,
 797 395–409. doi: <https://doi.org/10.1657/AAAR0014-023>
- 798 Chen, R., Duan, K., Shang, W., Shi, P., Meng, Y., & Zhang, Z. (2022). In-
 799 crease in seasonal precipitation over the tibetan plateau in the 21st century
 800 projected using cmip6 models. *Atmospheric Research*, *277*, 106306. doi:
 801 <https://doi.org/10.1016/j.atmosres.2022.106306>
- 802 Chen, R., Li, H., Wang, X., Gou, X., Yang, M., & Wan, G. (2022). Surface air
 803 temperature changes over the tibetan plateau: Historical evaluation and future
 804 projection based on cmip6 models. *Geoscience Frontiers*, *13*, 101452. doi:
 805 <https://doi.org/10.1016/j.gsf.2022.101452>
- 806 Chen, R., von Deimling, T. S., Boike, J., Wu, Q., & Langer, M. (2023). Simulating
 807 the thermal regime of a railway embankment structure on the tibetan plateau
 808 under climate change. *Cold Regions Science and Technology*, *212*, 103881. doi:
 809 <https://doi.org/10.1016/j.coldregions.2023.103881>
- 810 Chen, T., & Guestrin, C. (2016). Xgboost: A scalable tree boosting system. In
 811 *Proceedings of the 22nd ACM SIGKDD international conference on knowledge*
 812 *discovery and data mining* (p. 785–794). New York, NY, USA: Association
 813 for Computing Machinery. Retrieved from <https://doi.org/10.1145/2939672.2939785> doi: 10.1145/2939672.2939785

- Chen, Y., Cheng, X., Liu, A., Chen, Q., & Wang, C. (2023). Tracking lake drainage events and drained lake basin vegetation dynamics across the arctic. *Nature Communications*, 14, 7359. doi: <https://doi.org/10.1038/s41467-023-43207-0>
- Cuo, L., Zhang, Y., & Li, N. (2022). Historical and future vegetation changes in the degraded frozen soil and the entire tibetan plateau and climate drivers. *Journal of Geophysical Research: Biogeosciences*, 127, e2022JG006987. doi: <https://doi.org/10.1029/2022JG006987>
- Dai, L., Che, T., Xie, H., & Wu, X. (2018). Estimation of snow depth over the qinghai-tibetan plateau based on amsr-e and modis data. *Remote Sensing*, 10, 1989. doi: <https://doi.org/10.3390/rs10121989>
- Dai, Y., Shangguan, W., Duan, Q., Liu, B., Fu, S., & Niu, G. (2013). Development of a china dataset of soil hydraulic parameters using pedotransfer functions for land surface modeling. *Journal of Hydrometeorology*, 14, 869–887.
- Dai, Y., Wei, N., Yuan, H., Zhang, S., Shangguan, W., Liu, S., ... Xin, Y. (2019). Evaluation of soil thermal conductivity schemes for use in land surface modeling. *Journal of Advances in Modeling Earth Systems*, 11, 3454–3473. doi: <https://doi.org/10.1029/2019MS001723>
- Dai, Y., Xin, Q., Wei, N., Zhang, Y., Shangguan, W., Yuan, H., ... Lu, X. (2019). A global high-resolution data set of soil hydraulic and thermal properties for land surface modeling. *Journal of Advances in Modeling Earth Systems*, 11, 2996–3023. doi: <https://doi.org/10.1029/2019MS001784>
- de Vrese, P., Georgievski, G., Rouco, J. F. G., Notz, D., Stacke, T., Steinert, N. J., ... Brovkin, V. (2023). Representation of soil hydrology in permafrost regions may explain large part of inter-model spread in simulated arctic and subarctic climate. *The Cryosphere*, 17, 2095–2118. doi: <https://doi.org/10.5194/tc-17-2095-2023>
- Didan, K. (2015). *Mod13a2 modis/terra vegetation indices 16-day l3 global 1km sin grid v006*. doi: <https://doi.org/10.5067/MODIS/MOD13A2.061>
- Ding, J., Chen, L., Ji, C., Hugelius, G., Li, Y., Liu, L., ... Yang, Y. (2017). Decadal soil carbon accumulation across tibetan permafrost regions. *Nature Geoscience*, 10, 420–424. doi: <https://doi.org/10.1038/ngeo2945>
- Ehlers, T. A., Chen, D., Appel, E., Bolch, T., Chen, F., Diekmann, B., ... Zhu, L. (2022). Past, present, and future geo-biosphere interactions on the tibetan plateau and implications for permafrost. *Earth-Science Reviews*, 234, 104197. doi: <https://doi.org/10.1016/j.earscirev.2022.104197>
- Fan, Y., Li, H., & Miguez-Macho, G. (2013). Global patterns of groundwater table depth. *Science*, 339, 940–943. doi: <https://doi.org/10.1126/science.1229881>
- Gagnon, M., Domine, F., & Boudreau, S. (2019). The carbon sink due to shrub growth on arctic tundra: a case study in a carbon-poor soil in eastern canada. *Environmental Research Communications*, 1, 091001. doi: <https://doi.org/10.1088/2515-7620/ab3cdd>
- Gao, J., Jiao, K., Wu, S., Ma, D., Zhao, D., Yin, Y., & Dai, E. (2017). Past and future effects of climate change on spatially heterogeneous vegetation activity in china. *Earth's Future*, 5, 679–692. doi: <https://doi.org/10.1002/2017EF000573>
- Gao, Q., Guo, Y., Xu, H., Ganjurjav, H., Li, Y., Wan, Y., ... Liu, S. (2016). Climate change and its impacts on vegetation distribution and net primary productivity of the alpine ecosystem in the qinghai-tibetan plateau. *Science of The Total Environment*, 554–555, 34–41. doi: <https://doi.org/10.1016/j.scitotenv.2016.02.131>
- Gao, T., Zhang, Y., Kang, S., Abbott, B. W., Wang, X., Zhang, T., ... Gustafsson, Ö. (2021). Accelerating permafrost collapse on the eastern tibetan plateau. *Environmental Research Letters*, 16, 054023. doi: <https://doi.org/10.1088/1748-9326/abf7f0>
- Gao, Y., Luo, D., Chen, F., Lei, W., & Jin, H. (2023). Characteristics of the thermal

- regime and freeze-thaw cycles on the ground surface in permafrost regions in
the headwater area of the yellow river. *Acta Geographica Sinica*, 78, 604–619.
doi: <https://geog.com.cn/EN/10.11821/dlx202303007>
- Grünberg, I., Wilcox, E. J., Zwieback, S., Marsh, P., & Boike, J. (2020). Linking
tundra vegetation, snow, soil temperature, and permafrost. *Biogeosciences*, 17,
4261–4279. doi: <https://doi.org/10.5194/bg-17-4261-2020>
- Guo, D., & Wang, H. (2013). Simulation of permafrost and seasonally frozen ground
conditions on the tibetan plateau, 1981–2010. *Journal of Geophysical Research: Atmospheres*, 118, 5216–5230. doi: <https://doi.org/10.1002/jgrd.50457>
- Guo, J., Zhai, L., Sang, H., Cheng, S., & Li, H. (2023). Effects of hydrothermal
factors and human activities on the vegetation coverage of the qinghai-tibet plateau.
Scientific Reports, 13, 12488. doi: <https://doi.org/10.1038/s41598-023-39761-8>
- Guo, W., Liu, S., Xu, J., Wu, L., Shangguan, D., Yao, X., ... Jiang, Z. (2015).
The second chinese glacier inventory: data, methods and results. *Journal of
Glaciology*, 61, 357–372. doi: <https://doi.org/10.3189/2015JoG14J209>
- Gupta, H. V., Kling, H. K., K., Yilmaz, & Martinez, G. F. (2009). Decomposition
of the mean squared error and nse performance criteria: Implications for
improving hydrological modelling. *Journal of Hydrology*, 377, 80–91. doi:
<https://doi.org/10.1016/j.jhydrol.2009.08.003>
- Hamm, A., Magnússon, R. Í., Khattak, A. J., & Frampton, A. (2023). Continentiality
determines warming or cooling impact of heavy rainfall events on
permafrost. *Nature Communications*, 14, 3578. doi: <https://doi.org/10.1038/s41467-023-39325-4>
- Hawinkel, P., Thiery, W., Lhermitte, S., Swinnen, E., Verbist, B., Orshoven, J. V.,
& Muys, B. (2016). Vegetation response to precipitation variability in east
africa controlled by biogeographical factors. *Journal of Geophysical Research:
Biogeosciences*, 121, 2422–2444. doi: <https://doi.org/10.1002/2016JG003436>
- He, J., Yang, K., Tang, W., Lu, H., Qin, J., Chen, Y., & Li, X. (2020). The first
high-resolution meteorological forcing dataset for land process studies over
china. *Scientific Data*, 7, 25. doi: <https://doi.org/10.1038/s41597-020-0369-y>
- Heijmans, M. M. P. D., Magnússon, R. Í., Lara, M. J., Frost, G. V., Myers-Smith,
I. H., van Huissteden, J., ... Limpens, J. (2022). Tundra vegetation change
and impacts on permafrost. *Nature Reviews Earth & Environment*, 3, 68–84.
doi: <https://doi.org/10.1038/s43017-021-00233-0>
- Higgins, S. I., Conradi, T., & Muhoko, E. (2023). Shifts in vegetation activity of ter-
restrial ecosystems attributable to climate trends. *Nature Geoscience*, 16, 147–
153. doi: <https://doi.org/10.1038/s41561-022-01114-x>
- Jin, X., Jin, H., Iwahana, G., Marchenko, S. S., Luo, D., Li, X., & Liang, S.
(2021). Impacts of climate-induced permafrost degradation on vegeta-
tion: A review. *Advances in Climate Change Research*, 12, 29–47. doi:
<https://doi.org/10.1016/j.accre.2020.07.002>
- Jin, Z., You, Q., Zuo, Z., Li, M., Sun, G., Pepin, N., & Wang, L. (2023). Weakening
amplification of grassland greening to transpiration fraction of evapotranspira-
tion over the tibetan plateau during 2001-2020. *Agricultural and Forest Meteorology*, 341, 109661. doi: <https://doi.org/10.1016/j.agrformet.2023.109661>
- Ke, G., Meng, Q., Finley, T., Wang, T., Chen, W., Ma, W., ... Liu, T. (2017).
Lightgbm: A highly efficient gradient boosting decision tree. In *Proceedings
of the 31st international conference on neural information processing systems*
(pp. 3149–3157). Red Hook, NY, USA: Curran Associates Inc.
- Kondylatos, S., Prapas, I., Ronco, M., Papoutsis, I., Camps-Valls, G., Piles, M.,
... Carvalhais, N. (2022). Wildfire danger prediction and understanding
with deep learning. *Geophysical Research Letters*, e2022GL099368. doi:
<https://doi.org/10.1029/2022GL099368>
- Kong, Z., Liang, H., Deng, M., Han, F., Yan, J., Deng, X., ... Wang, W. (2023).

- Past and projected future patterns of fractional vegetation coverage in china.
Science of The Total Environment, 902, 166133. doi: <https://doi.org/10.1016/j.scitotenv.2023.166133>
- Langer, M., Nitzbon, J., Groenke, B., Assmann, L.-M., von Deimling, T. S., Stuenzi, S. M., & Westermann, S. (2024). The evolution of arctic permafrost over the last 3 centuries from ensemble simulations with the cryogridlite permafrost model. *The Cryosphere*, 18, 363–385. doi: <https://doi.org/10.5194/tc-18-363-2024>
- Langer, M., von Deimling, T. S., Westermann, S., Rolph, R., Ralph, R., Antonova, S., ... Grosse, G. (2023). Thawing permafrost poses environmental threat to thousands of sites with legacy industrial contamination. *Nature Communications*, 14, 1721. doi: <https://doi.org/10.1038/s41467-023-37276-4>
- Lawrence, D. M., & Swenson, S. C. (2011). Permafrost response to increasing arctic shrub abundance depends on the relative influence of shrubs on local soil cooling versus large-scale climate warming. *Environmental Research Letters*, 6, 045504. doi: <https://doi.org/10.1088/1748-9326/6/4/045504>
- Li, H., Pan, X., Washakh, R. M. A., & Nie, X. (2024). A new method of diagnosing the historical and projected changes in permafrost on the tibetan plateau. *Earth's Future*, 12, e2023EF003897. doi: <https://doi.org/10.1029/2023EF003897>
- Li, J., Wu, C., nuelas, J. P., Ran, Y., & Zhang, Y. (2023). The start of frozen dates over northern permafrost regions with the changing climate. *Global Change Biology*, 29, 4556–4568. doi: <https://doi.org/10.1111/gcb.16752>
- Li, X., Zhang, K., & Li, X. (2022). Responses of vegetation growth to climate change over the tibetan plateau from 1982 to 2018. *Environmental Research Communications*, 4, 045007.
- Liu, L., Zhuang, Q., Zhao, D., Zheng, D., Kou, D., & Yang, Y. (2022). Permafrost degradation diminishes terrestrial ecosystem carbon sequestration capacity on the qinghai-tibetan plateau. *Global Biogeochemical Cycles*, 36, e2021GB007068. doi: <https://doi.org/10.1029/2021GB007068>
- Liu, W., Wang, G., Yu, M., Chen, H., & Jiang, Y. (2020). Multimodel future projections of the regional vegetation-climate system over east asia: Comparison between two ensemble approaches. *Journal of Geophysical Research: Atmospheres*, 125, e2019JD031967. doi: <https://doi.org/10.1029/2019JD031967>
- Loranty, M. M., Abbott, B. W., Blok, D., Douglas, T. A., Epstein, H. E., Forbes, B. C., ... Walker, D. A. (2018). Reviews and syntheses: Changing ecosystem influences on soil thermal regimes in northern high-latitude permafrost regions. *Biogeosciences*, 15, 5287–5313. doi: <https://doi.org/10.5194/bg-15-5287-2018>
- Lu, H., Zheng, D., Yang, K., & Yang, F. (2020). Last-decade progress in understanding and modeling the land surface processes on the tibetan plateau. *Hydrology and Earth System Sciences*, 24, 5745–5758. doi: <https://doi.org/10.5194/hess-24-5745-2020>
- Lucazeau, F. (2019). Analysis and mapping of an updated terrestrial heat flow data set. *Geochemistry, Geophysics, Geosystems*, 20, 4001–4024. doi: <https://doi.org/10.1029/2019GC008389>
- Luo, D., Jin, H., Jin, X., He, R., Li, X., Muskett, R. R., ... Romanovsky, V. E. (2018). Elevation-dependent thermal regime and dynamics of frozen ground in the bayan har mountains, northeastern qinghai-tibet plateau, southwest china. *Permafrost and Periglacial Processes*, 29, 257–270. doi: <https://doi.org/10.1002/ppp.1988>
- Mahowald, N., Lo, F., Zheng, Y., Harrison, L., Funk, C., Lombardozzi, D., & Goodale, C. (2016). Projections of leaf area index in earth system models. *Earth System Dynamics*, 7, 211–229. doi: <https://doi.org/10.5194/esd-7-211-2016>
- Mauclet, E., Agnan, Y., Hirst, C., Monhonval, A., Pereira, B., Vanduren, A., ...

- 983 Opfergelt, S. (2022). Changing sub-arctic tundra vegetation upon permafrost
 984 degradation: impact on foliar mineral element cycling. *Biogeosciences*, *19*,
 985 2333–2351. doi: <https://doi.org/10.5194/bg-19-2333-2022>
- 986 Mekonnen, Z. A., Riley, W. J., & Grant, R. F. (2018). Accelerated nutrient cy-
 987 cling and increased light competition will lead to 21st century shrub expansion
 988 in north american arctic tundra. *Journal of Geophysical Research: Bioge-
 989 osciences*, *123*, 1683–1701. doi: <https://doi.org/10.1029/2017JG004319>
- 990 Mu, C., Abbott, B. W., Norris, A. J., Mu, M., Fan, C., Chen, X., ... Wu, X.
 991 (2020). The status and stability of permafrost carbon on the tibetan
 992 plateau. *Earth-Science Reviews*, *211*, 103433. doi: <https://doi.org/10.1016/j.earscirev.2020.103433>
- 993 Mu, C., Abbott, B. W., Zhao, Q., Su, H., Wang, S., Wu, Q., ... Wu, X. (2017).
 994 Permafrost collapse shifts alpine tundra to a carbon source but reduces n₂o
 995 and ch₄ release on the northern qinghai-tibetan plateau. *Geophysical Research
 996 Letters*, *44*, 8945–8952. doi: <https://doi.org/10.1002/2017GL074338>
- 997 Mu, C., & Peng, X. (2022). *A synthesis dataset of frozen ground and soil carbon in
 998 heihe river basin qilian mountainous (2011–2020)*. National Tibetan Plateau
 1000 Data Center. doi: <https://doi.org/10.11888/Cryos.tpdC.272840>
- 1001 Müller, W. A., Jungclaus, J. H., Mauritsen, T., Baehr, J., Bittner, M., Budich, R.,
 1002 ... Marotzke, J. (2018). A higher-resolution version of the max planck insti-
 1003 tute earth system model (mpi-esm1.2-hr). *Journal of Advances in Modeling
 1004 Earth Systems*, *10*, 1383–1413. doi: <https://doi.org/10.1029/2017MS001217>
- 1005 Muñoz-Sabater, J., Dutra, E., Agustí-Panareda, A., Albergel, C., Arduini, G., Bal-
 1006 samo, G., ... Thépaut, J.-N. (2021). Era5-land: a state-of-the-art global
 1007 reanalysis dataset for land applications. *Earth System Science Data*, *13*,
 1008 4349–4383. doi: <https://doi.org/10.5194/essd-13-4349-2021>
- 1009 Myers-Smith, I. H., Kerby, J. T., Phoenix, G. K., Bjerke, J. W., Epstein, H. E., Ass-
 1010 mann, J. J., ... Wipf, S. (2020). Complexity revealed in the greening of the
 1011 arctic. *Nature Climate Change*, *10*, 106–117. doi: <https://doi.org/10.1038/s41558-019-0688-1>
- 1012 Ni, J., Wu, T., Zhu, X., Hu, G., Zou, D., Wu, X., ... Yang, C. (2021). Simula-
 1013 tion of the present and future projection of permafrost on the qinghai-tibet
 1014 plateau with statistical and machine learning models. *Journal of Geophysical
 1015 Research: Atmospheres*, *126*, e2020JD033402. doi: <https://doi.org/10.1029/2020JD033402>
- 1016 Nitzbon, J., Krinner, G., von Deimling, T. S., Werner, M., & Langer, M. (2023).
 1017 First quantification of the permafrost heat sink in the earth's climate sys-
 1018 tem. *Geophysical Research Letters*, *50*, e2022GL102053. doi: <https://doi.org/10.1029/2022GL102053>
- 1019 Nitzbon, J., Langer, M., Martin, L. C. P., Westermann, S., von Deimling, T. S., &
 1020 Boike, J. (2021). Effects of multi-scale heterogeneity on the simulated evolu-
 1021 tion of ice-rich permafrost lowlands under a warming climate. *The Cryosphere*,
 1022 *15*, 1399–1422. doi: <https://doi.org/10.5194/tc-15-1399-2021>
- 1023 Nitzbon, J., Langer, M., Westermann, S., Martin, L., Aas, K. S., & Boike, J.
 1024 (2019). Pathways of ice-wedge degradation in polygonal tundra under
 1025 different hydrological conditions. *The Cryosphere*, *13*, 1089–1123. doi:
 1026 <https://doi.org/10.5194/tc-13-1089-2019>
- 1027 Nitze, I., Grosse, G., Jones, B. M., Romanovsky, V. E., & Boike, J. (2018). Re-
 1028 mote sensing quantifies widespread abundance of permafrost region distur-
 1029 bances across the arctic and subarctic. *Nature Communications*, *9*, 5423. doi:
 1030 <https://doi.org/10.1038/s41467-018-07663-3>
- 1031 Obu, J., Westermann, S., Bartsch, A., Berdnikov, N., Christiansen, H. H., Dasht-
 1032 seren, A., ... Zou, D. (2019). Northern hemisphere permafrost map based
 1033 on ttop modelling for 2000–2016 at 1km² scale. *Earth-Science Reviews*, *193*,
 1034 299–316. doi: <https://doi.org/10.1016/j.earscirev.2019.04.023>

- 1038 Orsolini, Y., Wegmann, M., Dutra, E., Liu, B., Balsamo, G., Yang, K., ... Arduini,
 1039 G. (2019). Evaluation of snow depth and snow cover over the tibetan plateau
 1040 in global reanalyses using in situ and satellite remote sensing observations. *The
 1041 Cryosphere*, *13*, 2221–2239. doi: <https://doi.org/10.5194/tc-13-2221-2019>
- 1042 Pang, G., Chen, D., Wang, X., & Lai, H. (2022). Spatiotemporal variations of land
 1043 surface albedo and associated influencing factors on the tibetan plateau. *Sci-
 1044 ence of The Total Environment*, *804*, 150100. doi: [https://doi.org/10.1016/j.scitotenv.2021.150100](https://doi.org/10.1016/j.

 1045 scitotenv.2021.150100)
- 1046 Pang, Y., Zou, K., Guo, X., Chen, Y., Zhao, J., Zhou, F., ... Yang, G. (2022).
 1047 Geothermal regime and implications for basin resource exploration in the
 1048 qaidam basin, northern tibetan plateau. *Journal of Asian Earth Sciences*, *239*,
 1049 105400. doi: <https://doi.org/10.1016/j.jseas.2022.105400>
- 1050 Pearson, R. G., Phillips, S. J., Loranty, M. M., Beck, P. S. A., Damoulas, T.,
 1051 Knight, S. J., & Goetz, S. J. (2013). Shifts in arctic vegetation and associ-
 1052 ated feedbacks under climate change. *Nature Climate Change*, *3*, 673–677. doi:
 1053 <https://doi.org/10.1038/nclimate1858>
- 1054 Piao, S., Wang, X., Park, T., Chen, C., Lian, X., He, Y., ... Myneni, R. B. (2020).
 1055 Characteristics, drivers and feedbacks of global greening. *Nature Reviews Earth
 1056 & Environment*, *1*, 14–27. doi: <https://doi.org/10.1038/s43017-019-0001-x>
- 1057 Prager, C. M., Boelman, N. T., Eitel, J. U. H., Gersony, J. T., Greaves, H. E.,
 1058 Heskel, M. A., ... Griffin, K. L. (2020). A mechanism of expansion: arctic de-
 1059 ciduous shrubs capitalize on warming-induced nutrient availability. *Oecologia*,
 1060 *192*, 671–685. doi: <https://doi.org/10.1007/s00442-019-04586-8>
- 1061 Qin, Y., Wu, T., Zhao, L., Wu, X., Li, R., Xie, C., ... Hao, J. (2017). Numerical
 1062 modeling of the active layer thickness and permafrost thermal state across
 1063 qinghai-tibetan plateau. *Journal of Geophysical Research: Atmospheres*, *122*,
 1064 11604–11620. doi: <https://doi.org/10.1002/2017JD026858>
- 1065 Ran, Y., Cheng, G., Dong, Y., Hjort, J., Lovecraft, A. L., Kang, S., ... Li, X.
 1066 (2022). Permafrost degradation increases risk and large future costs of in-
 1067 frastructure on the third pole. *Communications Earth & Environment*, *3*, 238.
 1068 doi: <https://doi.org/10.1038/s43247-022-00568-6>
- 1069 Ran, Y., Li, X., & Cheng, G. (2018). Climate warming over the past half century
 1070 has led to thermal degradation of permafrost on the qinghai-tibet plateau. *The
 1071 Cryosphere*, *12*, 595–608. doi: <https://doi.org/10.5194/tc-12-595-2018>
- 1072 Ran, Y., Li, X., Cheng, G., Che, J., Aalto, J., Karjalainen, O., ... Chang, X.
 1073 (2022). New high-resolution estimates of the permafrost thermal state and
 1074 hydrothermal conditions over the northern hemisphere. *Earth System Science
 1075 Data*, *14*, 865–884. doi: <https://doi.org/10.5194/essd-14-865-2022>
- 1076 Ran, Y., Li, X., Cheng, G., Nan, Z., Che, J., Sheng, Y., ... Wu, X. (2021). Mapping
 1077 the permafrost stability on the tibetan plateau for 2005–2015. *Science China
 1078 Earth Sciences*, *64*, 62–79. doi: <https://doi.org/10.1007/s11430-020-9685-3>
- 1079 Semmler, T., Danilov, S., Gierz, P., Goessling, H. F., Hegewald, J., Hinrichs, C., ...
 1080 Jung, T. (2020). Simulations for cmip6 with the awi climate model awi-cm-1-1.
 1081 *Journal of Advances in Modeling Earth Systems*, *12*, e2019MS002009. doi:
 1082 <https://doi.org/10.1029/2019MS002009>
- 1083 Sha, H., Lina, T., P, H. J., Yang, W., & Guofan, S. (2020). A commentary re-
 1084 view on the use of normalized difference vegetation index (ndvi) in the era
 1085 of popular remote sensing. *Journal of Forestry Research*, *32*, 1–6. doi:
 1086 <https://doi.org/10.1007/s11676-020-01155-1>
- 1087 Shen, C., Appling, A. P., Gentine, P., Bandai, T., Gupta, H., Tartakovsky, A., ...
 1088 Lawson, K. (2023). Differentiable modelling to unify machine learning and
 1089 physical models for geosciences. *Nature Reviews Earth & Environment*, *4*,
 1090 552–567. doi: <https://doi.org/10.1038/s43017-023-00450-9>
- 1091 Shen, M., Wang, S., Jiang, N., Sun, J., Cao, R., Ling, X., ... Fu, B. (2022). Plant
 1092 phenology changes and drivers on the qinghai-tibetan plateau. *Nature Re-*

- 1093 *views Earth & Environment*, 3, 633–651. doi: <https://doi.org/10.1038/s43017-022-00317-5>
- 1094 Shi, S., Wang, P., Zhan, X., Han, J., Guo, M., & Wang, F. (2023). Warming and in-
1095 creasing precipitation induced greening on the northern qinghai-tibet plateau.
1096 *Catena*, 233, 107483. doi: <https://doi.org/10.1016/j.catena.2023.107483>
- 1097 Smith, S. L., O'Neill, H. B., Isaksen, K., Noetzli, J., & Romanovsky, V. E. (2022).
1098 The changing thermal state of permafrost. *Nature Reviews Earth & Environ-
1099 ment*, 3, 10–23. doi: <https://doi.org/10.1038/s43017-021-00240-1>
- 1100 Song, L., Wang, L., Zhou, J., Luo, D., & Li, X. (2022). Divergent runoff impacts
1101 of permafrost and seasonally frozen ground at a large river basin of tibetan
1102 plateau during 1960–2019. *Environmental Research Letters*, 17, 124038. doi:
1103 <https://doi.org/10.1088/1748-9326/aca4eb>
- 1104 Stuenzi, S. M., Boike, J., Cable, W., Herzschuh, U., Kruse, S., Pestryakova, L. A.,
1105 ... Langer, M. (2021). Variability of the surface energy balance in permafrost-
1106 underlain boreal forest. *Biogeosciences*. doi: <https://doi.org/10.5194/bg-18-343-2021>
- 1107 Stuenzi, S. M., Boike, J., Gädke, A., Herzschuh, U., Kruse, S., Pestryakova, L. A.,
1108 ... Langer, M. (2021). Sensitivity of ecosystem-protected permafrost under
1109 changing boreal forest structures. *Environmental Research Letters*, 16, 085045.
1110 doi: <https://doi.org/10.1088/1748-9326/ac153d>
- 1111 Teng, H., Luo, Z., Chang, J., Shi, Z., Chen, S., Zhou, Y., ... Tian, H. (2021).
1112 Climate change-induced greening on the tibetan plateau modulated by moun-
1113 tainous characteristics. *Environmental Research Letters*, 16, 064064. doi:
1114 <https://doi.org/10.1088/1748-9326/abfeeb>
- 1115 Ukkonen, P., & Mäkelä, A. (2019). Evaluation of machine learning classifiers for pre-
1116 dicting deep convection. *Journal of Advances in Modeling Earth Systems*, 11,
1117 1784–1802. doi: <https://doi.org/10.1029/2018MS001561>
- 1118 van der Kolk, H.-J., Heijmans, M. M. P. D., van Huissteden, J., Pullens, J. W. M.,
1119 & Berendse, F. (2016). Potential arctic tundra vegetation shifts in response to
1120 changing temperature, precipitation and permafrost thaw. *Biogeosciences*, 13,
1121 6229–6245. doi: <https://doi.org/10.5194/bg-13-6229-2016>
- 1122 Veigel, N., Kreibich, H., & Cominola, A. (2023). Interpretable machine learn-
1123 ing reveals potential to overcome reactive flood adaptation in the continen-
1124 tal us. *Earth's Future*, 11, e2023EF003571. doi: <https://doi.org/10.1029/2023EF003571>
- 1125 Wang, J., & Liu, D. (2022). Vegetation green-up date is more sensitive to
1126 permafrost degradation than climate change in spring across the north-
1127 ern permafrost region. *Global Change Biology*, 28, 1569–1582. doi:
1128 <https://doi.org/10.1111/gcb.16011>
- 1129 Wang, T., Yang, D., Yang, Y., Piao, S., Li, X., Cheng, G., & Fu, B. (2020). Per-
1130 ma frost thawing puts the frozen carbon at risk over the tibetan plateau. *Sci-
1131 ence Advances*, 6, eaaz3513. doi: <https://doi.org/10.1126/sciadv.aaz3513>
- 1132 Wang, T., Yang, D., Yang, Y., Zheng, G., Jin, H., Li, X., ... Cheng, G. (2023).
1133 Pervasive permafrost thaw exacerbates future risk of water shortage across the
1134 tibetan plateau. *Earth's Future*, 11, e2022EF003463. doi: <https://doi.org/10.1029/2022EF003463>
- 1135 Wang, T., Yang, D., Zheng, G., & Shi, R. (2022). Possible negative effects of ear-
1136 lier thaw onset and longer thaw duration on vegetation greenness over the
1137 tibetan plateau. *Agricultural and Forest Meteorology*, 326, 109192. doi:
1138 <https://doi.org/10.1016/j.agrformet.2022.109192>
- 1139 Wang, W., Rinke, A., Moore, J. C., Cui, X., Ji, D., Li, Q., ... Decharme, B.
1140 (2016). Diagnostic and model dependent uncertainty of simulated tibetan
1141 permafrost area. *The Cryosphere*, 10, 287–306. doi: <https://doi.org/10.5194/tc-10-287-2016>
- 1142 Wang, W., Yang, K., Zhao, L., Zheng, Z., Lu, H., Mamtimin, A., ... Moore, J. C.

- 1148 (2020). Characterizing surface albedo of shallow fresh snow and its importance
 1149 for snow ablation on the interior of the tibetan plateau. *Journal of Hydrometeorology*, 21, 815–827. doi: <https://doi.org/10.1175/JHM-D-19-0193.1>
- 1150
- 1151 Wang, X., Ran, Y., Pang, G., Chen, D., Su, B., Chen, R., ... Luo, D. (2022).
 1152 Contrasting characteristics, changes, and linkages of permafrost between
 1153 the arctic and the third pole. *Earth-Science Reviews*, 230, 104042. doi:
 1154 <https://doi.org/10.1016/j.earscirev.2022.104042>
- 1155 Wang, Y., Xiao, J., Ma, Y., Ding, J., Chen, X., Ding, Z., & Luo, Y. (2023). Per-
 1156 sistent and enhanced carbon sequestration capacity of alpine grasslands on
 1157 earth's third pole. *Science Advances*, 9, eade6875. doi: <https://doi.org/10.1126/sciadv.ade6875>
- 1158 Wang, Z., Wang, Q., Zhao, L., Wu, X., Yue, G., Zou, D., ... Zhang, Y. Z. . L.
 1159 (2016). Mapping the vegetation distribution of the permafrost zone on the
 1160 qinghai-tibet plateau. *Journal of Mountain Science*, 13, 1035–1046. doi:
 1161 <https://doi.org/10.1007/s11629-015-3485-y>
- 1162 Wei, D., Qi, Y., Ma, Y., & Wang, X. (2021). Plant uptake of co₂ outpaces losses
 1163 from permafrost and plant respiration on the tibetan plateau. *Proceedings of
 1164 the National Academy of Sciences*, 118, e2015283118. doi: <https://doi.org/10.1073/pnas.2015283118>
- 1165 Wei, Y., Lu, H., Wang, J., Wang, X., & Sun, J. (2022). Dual influence of climate
 1166 change and anthropogenic activities on the spatiotemporal vegetation dynam-
 1167 ics over the qinghai-tibetan plateau from 1981 to 2015. *Earth's Future*, 10,
 1168 e2021EF002566. doi: <https://doi.org/10.1029/2021EF002566>
- 1169 Westermann, S., Ingeman-Nielsen, T., Scheer, J., Aalstad, K., Aga, J., Chaud-
 1170 hary, N., ... Langer, M. (2023). The cryogrid community model (version
 1171 1.0) – a multi-physics toolbox for climate-driven simulations in the terres-
 1172 trial cryosphere. *Geoscientific Model Development*, 16, 2607–2647. doi:
 1173 <https://doi.org/10.5194/gmd-16-2607-2023>
- 1174 Westermann, S., Langer, M., Boike, J., Heikenfeld, M., Peter, M., Etzelmüller, B.,
 1175 & Krinner, G. (2016). Simulating the thermal regime and thaw processes
 1176 of ice-rich permafrost ground with the land-surface model cryogrid3. *Geo-
 1177 scientific Model Development*, 9, 523–546. doi: <https://doi.org/10.5194/gmd-9-523-2016>
- 1178 Wu, M., Chen, S., Chen, J., Xue, K., Chen, S., Wang, X., ... Wang, Y. (2021).
 1179 Reduced microbial stability in the active layer is associated with carbon loss
 1180 under alpine permafrost degradation. *Proceedings of the National Academy of
 1181 Sciences*, 118, e2025321118. doi: <https://doi.org/10.1073/pnas.2025321118>
- 1182 Wu, Q., & Zhang, T. (2008). Recent permafrost warming on the qinghai-tibetan
 1183 plateau. *Journal of Geophysical Research: Atmospheres*, 113, D13108. doi:
 1184 <https://doi.org/10.1029/2007JD009539>
- 1185 Wu, Q., & Zhang, T. (2010). Changes in active layer thickness over the qinghai-
 1186 tibetan plateau from 1995 to 2007. *Journal of Geophysical Research: Atmo-
 1187 spheres*, 115, D09107. doi: <https://doi.org/10.1029/2009JD012974>
- 1188 Wu, Q., Zhang, T., & Liu, Y. (2020). Thermal state of the active layer and per-
 1189 ma frost along the qinghai-xizang (tibet) railway from 2006 to 2010. *The
 1190 Cryosphere*, 31, 417–428. doi: <https://doi.org/10.1002/ppp.2059>
- 1191 Xia, Z., Huang, L., Fan, C., Jia, S., Lin, Z., Liu, L., ... Zhang, T. (2022). Retro-
 1192 gressive thaw slumps along the qinghai-tibet engineering corridor: a com-
 1193 prehensive inventory and their distribution characteristics. *Earth System Science
 1194 Data*, 14, 3875–3887. doi: <https://doi.org/10.5194/essd-14-3875-2022>
- 1195 Yan, F., Shangguan, W., Zhang, J., & Hu, B. (2020). Depth-to-bedrock map of
 1196 china at a spatial resolution of 100 meters. *Scientific Data*, 7, 2. doi: <https://doi.org/10.1038/s41597-019-0345-6>
- 1197 Yang, J., Xin, Z., Huang, Y., & Liang, X. (2023). Multi-source remote sensing data
 1198 shows a significant increase in vegetation on the tibetan plateau since 2000.
- 1199
- 1200
- 1201
- 1202

- 1203 *Progress in Physical Geography: Earth and Environment*, 47, 597–624. doi:
1204 <https://doi.org/10.1177/03091333221148052>

1205 Yi, S., Wang, X., Qin, Y., Xiang, B., & Ding, Y. (2014). Responses of alpine grass-
1206 land on qinghai-tibetan plateau to climate warming and permafrost degrada-
1207 tion: a modeling perspective. *Environmental Research Letters*, 9, 074014. doi:
1208 <https://doi.org/10.1088/1748-9326/9/7/074014>

1209 Yin, G., Niu, F., Lin, Z., Luo, J., & Liu, M. (2021). Data-driven spatiotemporal pro-
1210 jections of shallow permafrost based on cmip6 across the qinghai-tibet plateau
1211 at 1 km² scale. *Advances in Climate Change Research*, 12, 814—827. doi:
1212 <https://doi.org/10.1016/j.accre.2021.08.009>

1213 Zhang, G., Luo, W., Chen, W., & Zheng, G. (2019). A robust but variable lake ex-
1214 pansion on the tibetan plateau. *Science Bulletin*, 64, 1306–1309. doi: <https://doi.org/10.1016/j.scib.2019.07.018>

1215 Zhang, G., Nan, Z., Hu, N., Yin, Z., Zhao, L., Cheng, G., & Mu, C. (2022). Qinghai-
1216 tibet plateau permafrost at risk in the late 21st century. *Earth's Future*, 10,
1217 e2022EF002652. doi: <https://doi.org/10.1029/2022EF002652>

1218 Zhang, G., Nan, Z., Zhao, L., Liang, Y., & Cheng, G. (2021). Qinghai-tibet plateau
1219 wetting reduces permafrost thermal responses to climate warming. *Earth
1220 and Planetary Science Letters*, 562, 116858. doi: <https://doi.org/10.1016/j.epsl.2021.116858>

1221 Zhang, Q., Kong, D., Shi, P., Singh, V. P., & Sun, P. (2018). Vegetation phe-
1222 nology on the qinghai-tibetan plateau and its response to climate change
1223 (1982–2013). *Agricultural and Forest Meteorology*, 248, 408–417. doi:
1224 <https://doi.org/10.1016/j.agrformet.2017.10.026>

1225 Zhang, X., & Li, X. (2023). Three-dimensional differentiation of the contribution
1226 of climatic factors to vegetation change in the pan-tibetan plateau. *Journal of
1227 Geophysical Research: Biogeosciences*, 128, e2022JG007244. doi: <https://doi.org/10.1029/2022JG007244>

1228 Zhang, Y., Li, B., & Zheng, D. (2014). Datasets of the boundary and area of the ti-
1229 betan plateau. *Acta Geographica Sinica*, 69, 65–68. doi: <https://doi.org/10.11821/dlx2014S012>

1230 Zhang, Z., Wu, Q., Jiang, G., Gao, S., Chen, J., & Liu, Y. (2020). Changes in the
1231 permafrost temperatures from 2003 to 2015 in the qinghai-tibet plateau. *Cold
1232 Regions Science and Technology*, 169, 102904. doi: <https://doi.org/10.1016/j.coldregions.2019.102904>

1233 Zhao, L., Zou, D., Hu, G., Wu, T., Du, E., Liu, G., ... Cheng, G. (2021). A synthe-
1234 sis dataset of permafrost thermal state for the qinghai-tibet (xizang) plateau,
1235 china. *Earth System Science Data*, 13, 4207–4218. doi: <https://doi.org/10.5194/essd-13-4207-2021>

1236 Zhou, J., Zheng, Y., Song, C., Cheng, C., Gao, P., & Ye, S. (2022). *Vegetation map
1237 of qinghai tibet plateau in 1980s*. National Tibetan Plateau Data Center. doi:
1238 <https://doi.org/10.11888/Terre.tpdc.272385>

1239 Zou, D., Zhao, L., Sheng, Y., Chen, J., Hu, G., Wu, T., ... Cheng, G. (2017). A
1240 new map of permafrost distribution on the tibetan plateau. *The Cryosphere*, 11,
1241 2527–2542. doi: <https://doi.org/10.5194/tc-11-2527-2017>